Article

Mononuclear Lanthanide(III)-Salicylideneaniline Complexes: Synthetic, Structural, Spectroscopic, and Magnetic Studies †

Ioannis Mylonas-Margaritis [1], **Diamantoula Maniaki** [1], **Julia Mayans** [2], **Laura Ciammaruchi** [3], **Vlasoula Bekiari** [4] , **Catherine P. Raptopoulou** [5] , **Vassilis Psycharis** [5,]* , **Sotirios Christodoulou** [6,]* , **Albert Escuer** [2,]* and **Spyros P. Perlepes** [1,7,]*

[1] Department of Chemistry, University of Patras, 26504 Patras, Greece;
    ioannismylonasmargaritis@gmail.com (I.M.-M.); dia.maniaki@gmail.com (D.M.)
[2] Departament de Quimica Inorgànica i Orgànica, Secció Inorgànica and Institut de Nanociencia i
    Nanotecnologia (IN²UB), Universitat de Barcelona, Marti i Franquès 1-11, 08028 Barcelona, Spain;
    julia.mayans@qi.ub.edu
[3] Department of Solar Energy and Environmental Physics, Ben-Gurion University of the Negev,
    Midreshet Sede Boqer 8499000, Israel; laura.ciammaruchi@gmail.com
[4] Department of Fisheries and Aquaculture Technology, Technological Educational Institute of Western
    Greece, 30200 Messolonghi, Greece; mpekiari@teimes.gr
[5] Institute of Nanoscience and Nanotechnology, NCSR "Demokritos", 15310 Aghia Paraskevi Attikis, Greece;
    c.raptopoulou@inn.demokritos.gr
[6] ICFO-Institut de Ciencies Fotoniques, The Barcelona Institute of Nanoscience and Nanotechnology,
    Castelldefels, 08860 Barcelona, Spain
[7] Institute of Chemical Engineering Sciences, Foundation for Research and
    Technology-Hellas (FORTH/ICE-HT), Platani, PO Box 1414, 26504 Patras, Greece
*   Correspondence: v.psycharis@inn.demokritos.gr (V.P.); sotirios.christodoulou@icfo.eu (S.C.);
    albert.escuer@ub.edu (A.E.); perlepes@patreas.upatras.gr (S.P.P.); Tel.: +30-210-6503346 (V.P.);
    +34-93-5534166 (S.C.); +34-93-4039141 (A.E.); +30-2610-996730 (S.P.P.)
†   This article is dedicated to Professor Emeritus Christopher Landee, a great physicist whose collaboration
    with chemists had led to exciting results in the area of the magnetic properties of coordination complexes.

check for updates

Abstract: The reactions of hydrated lanthanide(III) [Ln(III)] nitrates and salicylideneaniline (salanH) have provided access to two families of mononuclear complexes depending on the reaction solvent used. In MeCN, the products are $[Ln(NO_3)_3(salanH)_2(H_2O)]\cdot MeCN$, and, in MeOH, the products are $[Ln(NO_3)_3(salanH)_2(MeOH)]\cdot(salanH)$. The complexes within each family are proven to be isomorphous. The structures of complexes $[Ln(NO_3)_3(salanH)_2(H_2O)]\cdot MeCN$ (Ln = Eu, **4**·MeCN_Eu, Ln = Dy, **7**·MeCN_Dy; Ln = Yb, **10**·MeCN_Yb) and $[Ln(NO_3)_3(salanH)_2(MeOH)]\cdot(salanH)$ (Ln = Tb, **17**_Tb; Ln = Dy, **18**_Dy) have been solved by single-crystal X-ray crystallography. In the five complexes, the Ln^{III} center is bound to six oxygen atoms from the three bidentate chelating nitrato groups, two oxygen atoms from the two monodentate zwitterionic salanH ligands, and one oxygen atom from the coordinated H_2O or MeOH group. The salanH ligands are mutually "*cis*" in **4**·MeCN_Eu, **7**·MeCN_Dy and **10**·MeCN_Yb while they are "*trans*" in **17**_Tb and **18**_Dy. The lattice salanH molecule in **17**_Tb and **18**_Dy is also in its zwitterionic form with the acidic H atom being clearly located on the imine nitrogen atom. The coordination polyhedra defined by the nine oxygen donor atoms can be described as spherical tricapped trigonal prisms in **4**·MeCN_Eu, **7**·MeCN_Dy, and **10**·MeCN_Yb and as spherical capped square antiprisms in **17**_Tb and **18**_Dy. Various intermolecular interactions build the crystal structures, which are completely different in the members of the two families. Solid-state IR data of the complexes are discussed in terms of their structural features. ^{1}H NMR data for the diamagnetic Y(III) complexes provide strong evidence that the compounds decompose in DMSO by releasing the coordinated salanH ligands. The solid complexes emit green

light upon excitation at 360 nm (room temperature) or 405 nm (room temperature). The emission is ligand-based. The solid Pr(III), Nd(III), Sm(III), Er(III), and Yb(III) complexes of both families exhibit Ln^{III}-centered emission in the near-IR region of the electromagnetic spectrum, but there is probably no efficient salanH→Ln^{III} energy transfer responsible for this emission. Detailed magnetic studies reveal that complexes **7·MeCN_Dy**, **17_Tb** and **18_Dy** show field-induced slow magnetic relaxation while complex $[Tb(NO_3)_3(salanH)_2(H_2O)]$·MeCN (**6·MeCN_Tb**) does not display such properties. The values of the effective energy barrier for magnetization reversal are 13.1 cm^{-1} for **7·MeCN_Dy**, 14.8 cm^{-1} for **17_Tb**, and 31.0 cm^{-1} for **18_Dy**. The enhanced/improved properties of **17_Tb** and **18_Dy**, compared to those of **6_Tb** and **7_Dy**, have been correlated with the different supramolecular structural features of the two families. The molecules $[Ln(NO_3)_3(salanH)_2(MeOH)]$ of complexes **17_Tb** and **18_Dy** are by far better isolated (allowing for better slow magnetic relaxation properties) than the molecules $[Ln(NO_3)_3(salanH)_2(H_2O)]$ in **6·MeCN_Tb** and **7·MeCN_Dy**. The perspectives of the present initial studies in the Ln(III)/salanH chemistry are discussed.

1. Introduction

The interdisciplinary field of Molecular Magnetism [1] has undergone revolutionary changes since the early 1990s when it was discovered that the 3-dimensional metal coordination cluster $[Mn_{12}O_{12}(O_2CMe)_{16}(H_2O)_4]$ could behave as a single-domain tiny magnet at a very low temperature [2–4]. This discovery gave birth to the currently "hot" area of Single-Molecule Magnetism. Currently trivalent lanthanides, Ln(III), have entered the area in a dynamic way [5–14] by virtue of their large magnetic moments and single-ion anisotropies. Mononuclear Ln(III) complexes are central "players" in this "game" because they represent one of the smallest, magnetically bi-stable units and can, thus, be considered as ideal candidates for high-density storage or quantum computing [5,6,10,15–33]. Mononuclear Ln(III) Single-Molecule Magnets (SMMs), which are often called Single-Ion Magnets (SIMs), have been reported with a blocking temperature (~60 K) approaching that of the liquid nitrogen [34–36]. The effective energy anisotropic barrier for magnetization reversal arises from the intrinsic electronic sub-level structure of the Stark components [5]. Such energy considerations depend on the subtle variation of several parameters. These include the Kramers/non-Kramers character of the Ln^{III} center, its oblate/prolate 4f-electron density, the geometry of the complex, the symmetry of the coordination sphere, and the donor strength of the donor atoms [5–8]. The relaxation of the magnetization may take place through various mechanisms, which are either spin-lattice processes (Raman, Orbach, direct relaxations) or the Quantum Tunneling of the Magnetization (QTM) process. After 10 years of intense research, the design synthetic criterion has been established and tested for Dy(III) complexes. Dy(III) SIMs are the most numerous because Dy^{III} has an odd number of 4f electrons (a Kramers' ion), which ensures that the ground state will always be bi-stable irrespective of the symmetry of the ligand field. The requirement for a successful Dy(III) SIM is a strongly axial ligand field. The coordination numbers that give rise to strong axial crystal fields are 1 and 2. Such Ln(III) complexes cannot be isolated, but extensive synthetic and magnetic experimental work has proven that the Dy^{III} coordination number can be higher (this is the usual situation) as long as the strong axial crystal field is supported by equational ligands that are weak donors.

In addition to their exciting magnetic properties, the Ln^{III} ions in their simple salts and complexes give rise to interesting photoluminescence properties arising from forbidden 4f-4f (or 4f-5d in the case of Ce^{III}) electronic transitions [37,38]. The low intensity of the 4f-4f transitions is a disadvantage and use of suitable organic ligand chromophores is required. Thus, many Ln(III) complexes exhibit sharp, intense emission lines upon UV light excitation because of the effective intermolecular transfers

from the coordinated ligand (which behaves as an antenna) into the emissive levels of the Ln^{III} ions that result in a radiative emission process [37–39]. Of particular interest are Ln(III) complexes such as Pr(III), Nd(III), Sm(III), Dy(III), Ho(III), Er(III), and Yb(III) ones that emit light in the near-IR region of the electromagnetic spectrum [40–43]. These Ln^{III} ions find a wide variety of applications in fluoroimmunoassays (Yb^{III}-based luminescence), telecommunications (Er^{III} ~1.54 μm), optical communication systems (Tm^{III} ~1.4 μm), optical amplifiers (Dy^{III}-based luminescence), and solid-state lasers (Nd^{III} ~1.06 μm, Ho ~2.09 μm).

Another modern topic of relevance to the present work in the chemistry of Ln(III) complexes is the simultaneous incorporation of both SIM and photoluminescence properties in the same complex [44]. The concurrence of emission and magnetic properties in such bifunctional (or hybrid) materials creates the possibility of tuning light emission by a magnetic field. The initial studies were focused on the isolation of emissive ferromagnets due to their applications in multimodal sensing and optoelectronics [45]. Luminescent SIMs are also of great scientific value for the in-depth investigation of the mechanisms that govern the magnetization relaxation in mononuclear Ln(III) complexes because photoluminescence studies can, in principle, allow scientists to determine spectroscopically the Stark sublevels of some Ln^{III} ions and compare them with those derived from the magnetic measurements. Excellent results on this topic are available in References [44,46–49].

Our groups have a long-standing, intense interest in the chemistry, magnetism, and photoluminescence of 4f-metal complexes [50–56] and recently our attention has focused on mononuclear emissive Ln(III) complexes exhibiting slow magnetization relaxation [57]. Our design synthetic strategy is to use ligands that act as terminal (either monodentate or chelating) and possess chromophores that can facilitate efficient energy transfer from their triplet state to the Ln^{III} ions' excited (i.e., emissive) levels. Potentially polydentate O and N-donor Schiff bases [58] often lead to dinuclear or polynuclear complexes [13,59–61]. Rather surprisingly, mononuclear Ln(III) complexes with simple bidentate ligands derived from the condensation of salicylaldehyde (and its derivatives) and aniline (and its derivatives) have escaped the attention of scientists. The general formula of these ligands, which have the empirical name anils, is shown in Scheme 1. When neutral (the deprotonated phenoxido oxygen atom can bridge two Ln^{III} ions and favor dinuclear species), these ligands are expected to behave as bidentate chelating, which leads to mononuclear complexes. Moreover, the presence of two aromatic rings per molecule makes these Schiff bases potential antennas for sensitizing Ln^{III}-based emission. Anils have written their own history in Physical Chemistry. The prototype, N-salicylideneaniline ($R_1 = R_2 = H$ in Scheme 1; salanH; the systematic name is 2-(phenyliminomethyl)phenol; alternative names already used are 2-hydroxybenzylideneaniline or phenylsalicylaldimine) is a well-known organic photochromic compound whose crystals change their color from orange to red upon UV irradiation and then back to orange upon thermal fading or VIS irradiation [62–65]. The mechanism responsible for the photochromic color change has been proposed to involve (Scheme 2): (a) conversion of the colorless enol (or enol-imine) form to the orange *cis*-keto (or *cis*-keto-amine) form with excited-state intramolecular proton transfer upon UV irradiation (keto-enol tautomerization), and (b) *cis-trans* isomerization to afford the red *trans*-keto form. Extensive studies have revealed that the photochromic behavior of salanH is related to its molecular conformation in the crystal. The dihedral angle between the two aromatic rings is a key parameter for the appearance of the photochromic properties.
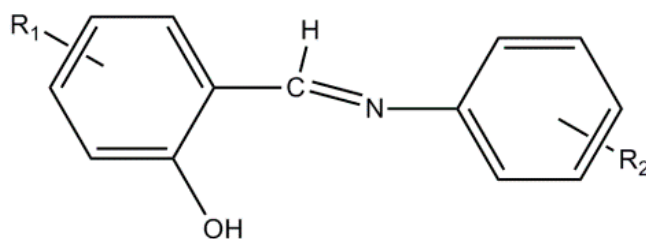
Scheme 1. General structural formula of anils. The ligand used in this work is N-salicylideneaniline (salanH, $R_1 = R_2 = H$).
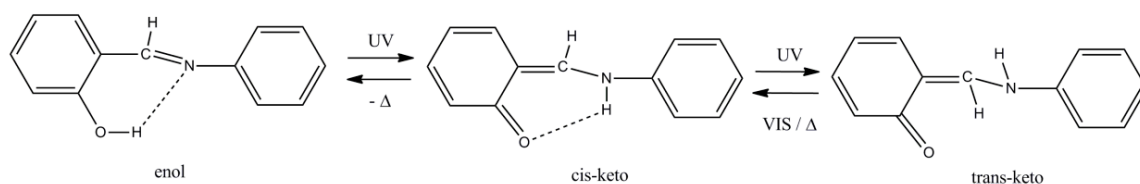
**Scheme 2.** Proposed mechanism for the photochromic behavior of salanH. Dashed lines indicate H bonds.

We have very recently reported the synthesis and characterization of the isomorphous complexes [Ln(NO$_3$)$_3$(5BrsalanH)$_2$(H$_2$O)]·MeCN where 5BrsalanH is *N*-(5-bromosalicylidene)aniline (R_1 = Br at the meta carbon position with respect to the OH-containing carbon atom) [57]. The Dy^{III} member of this family shows field-induced magnetic relaxation and emits green light upon excitation at ~340 nm with the photoluminescence being ligand-based. We report in this paper a logical continuation of this work, which involves the reactions of hydrated lanthanide(III) nitrates with neutral salanH (Scheme 1) and the prototype of the anil group of ligands. Our primary goals were: (i) The comparison of the coordination chemistry of salanH towards Ln(III) ions with that of 5BrsalanH [57] and (ii) the investigation of the magnetic properties of the Tb(III) and Dy(III) complexes and the possibility to observe slow magnetization relaxation, i.e., SIM properties and (iii) the study of the photoluminescence properties of selected compounds with emphasis on the possibilities to observe Ln^{III}-based emission and to record emission in the near-IR region. The ultimate goal was to isolate emissive SIMs. The salanH/salan$^-$ ligands have widely been used in transition and main group metal chemistries [66–74], but no Ln(III) complexes have been reported to date. The structural chemistry of the free salanH compound is exciting. This aromatic Schiff base forms two photochromic polymorphs, α_1 [75] and α_2 [76]. Both polymorphs feature non-coplanar phenyl rings and a planar, thermochromic polymorph, β [77]. A fourth planar polymorph was also reported two years ago [78]. All the four polymorphs are in the enol form featuring an intramolecular O-H···N H bond. It should be mentioned at this point that the phenomenon of thermochromism is related to that of the photochromism. Upon heating, the anils that are not photochromic in the crystalline state develop an absorbance spectrum resembling the spectrum of the colored photochromic solid with the process being the transformation of the enol form to the *cis*-keto form. The two phenomena are mutually exclusive.

Before closing the introduction, we would like to state that there is currently a renewed interest in the chemistry of mononuclear Ln(III)-Schiff base complexes because of two reasons: (a) There has been demonstrated that two and four electrons can be stored, respectively, in intramolecular and intermolecular C-C bonds formed by Ln(III)-assisted reduction of the imino group of Schiff base ligands, which shows that the latter can provide a promising alternative to amide and cyclopentadienyl ligands and open a novel route to the reductive chemistry of lanthanides [79] and (b) Yb(III) complexes with polydentate chelating Schiff bases are qubit candidates due to the very large splitting between the electronic ground doublet and the first excited crystal field state and their intrinsic slow paramagnetic relaxation [80] as well as candidates for novel coupled electronic qubit-nuclear qubit systems [81].

2. Results and Discussion

2.1. Synthetic Comments

Since we were interested in preparing mononuclear Ln(III) complexes with the neutral salanH ligand, we avoided the addition of an external base (e.g., NaOH, Et$_3$N, R$_4$NOH, etc.) in the reaction systems. Depending on the reaction solvent used, two families of mononuclear complexes were isolated. The 1:1 reactions of Ln(NO$_3$)$_3$ xH$_2$O or Y(NO$_3$)$_3$·6H$_2$O and salanH in MeCN gave orange crystals or microcrystalline powders in moderate to good yields (50% to 60%). Subsequent characterization revealed the formulation [Ln(NO$_3$)$_3$(salanH)$_2$(H$_2$O)]·MeCN (Ln = Pr, **1**·MeCN_Pr; Nd, **2**·MeCN_Nd; Sm, **3**·MeCN_Sm; Eu, **4**·MeCN_Eu; Gd, **5**·MeCN_Gd; Tb, **6**·MeCN_Tb; Dy, **7**·MeCN_Dy; Ho, **8**·MeCN_Ho; Er, **9**·MeCN_Er; Yb, **10**·MeCN_Yb), and [Y(NO$_3$)$_3$(salanH)$_2$(H$_2$O)]·MeCN (**11**·MeCN_Y). The crystals of **4**·MeCN_Eu, **7**·MeCN_Dy, and **10**·MeCN_Yb were of good quality and their structures were determined by single-crystal X-ray crystallography. The other complexes are proposed to be isomorphous with the structurally characterized compounds based on elemental analyses, IR spectra, powder X-ray patterns (pXRDs), and unit-cell determinations for selected complexes. Assuming that these mononuclear complexes are the only products from their corresponding reaction mixtures, their formation is summarized by Equation (1) where Ln stands for lanthanide or yttrium and x is 5 or 6.

$$Ln(NO_3)xH_2O + 2salanH + MeCN \overset{MeCN}{\rightarrow} [Ln(NO_3)_3(salanH)_2]MeCN + (x-1)H_2O \qquad (1)$$
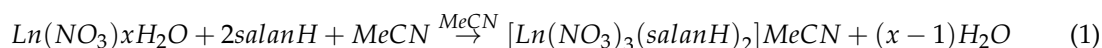
Analogous 1:1 reactions in MeOH gave yellowish orange solutions from which were subsequently precipitated orange crystals in moderate yields (40%–50%). The characterization of the products revealed the formulation [Ln(NO$_3$)$_3$(salanH)$_2$(MeOH)]·(salanH) [Ln = Pr, **12**_Pr; Nd, **13**_Nd; Sm, **14**_Sm; Eu, **15**_Eu; Gd, **16**_Gd; Tb, **17**_Tb; Dy, **18**_Dy; Ho, **19**_Ho; Er, **20**_Er; Yb, **21**_Yb), and [Y(NO$_3$)$_3$(salanH)$_2$(MeOH)]·(salanH) (**22**_Y). The crystals of **17**_Tb and **18**_Dy proved to be of X-ray quality and their structures were solved by single-crystal X-ray crystallography. Elemental analyses, IR spectra, pXRDs, and unit cell determinations for selected samples make us strongly believe that the other complexes are isomorphous with the structurally characterized compounds. Assuming that these mononuclear complexes are the only products from their corresponding reaction systems (this is not entirely correct, *vide infra*). Their formation can be represented by Equation (2) where Ln stands for lanthanide or yttrium and x is 5 or 6. Further points of synthetic interest are reported in the "Supplementary Materials" section.

$$Ln(NO_3)xH_2O + 3salanH + MeOH \overset{MeOH}{\rightarrow} [Ln(NO_3)_3(salanH)_2MeOH](salanH) + xH_2O \qquad (2)$$
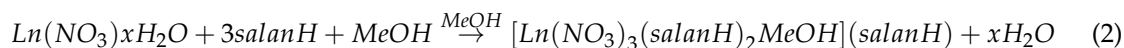
2.2. Conventional Characterization of the Complexes

The analytical data of well dried samples of complexes **1**·MeCN_Pr–**11**·MeCN_Y correspond to the formulation [Ln(NO$_3$)$_3$(salanH)$_2$(H$_2$O)]·yMeCN (y = 0–0.4). On the contrary, the analytical data of well dried samples of complexes **12**_Pr–**22**_Y correspond to the crystallographic formula [Ln(NO$_3$)$_3$(salanH)$_2$(MeOH)]·(salanH).

The samples used for the measurements are pure as proven by their pXRDs (Figures 1 and S1). In the case of **12**_Pr–**22**_Y, the experimental patterns of all compounds are identical with the simulated ones for the structurally characterized compounds **17**_Tb and **18**_Dy. In the case of **1**·MeCN_Pr–**11**·MeCN_Y, the slight differences between the experimental and theoretical (as derived from the cifs) patterns are due to the presence of one solvate MeCN molecule per molecule of complex, which is completely or partially lost in the dried samples used for the pXRD measurements. We also calculated the pattern of complex **4**·MeCN_Eu after removing the solvent atoms from the cif. Its similarity with the experimental pattern has slightly improved (Figure S2).

A full spectroscopic discussion (IR for all complexes, ^{1}H NMR for the Y^{III} complexes, and diffuse reflectance for selected complexes) is presented in the "Supplementary Materials" section. Representative spectra are shown in Figures S2–S7.
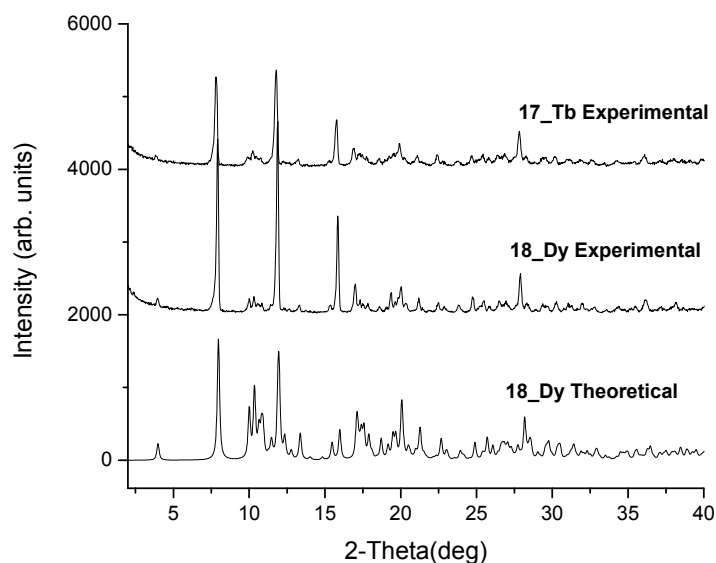
Figure 1. Experimental X-ray diffraction patterns of freshly prepared and well dried powders of complexes **17**_Tb and **18**_Dy. The simulated pattern of the structurally characterized Dy(III) complex **18**_Dy (labelled as **18**_Dy Theoretical) is also shown.

2.3. Description of Structures

The structures of complexes **4**·MeCN_Eu, **7**·MeCN_Dy, **10**·MeCN_Yb, **17**_Tb, and **18**_Dy have been fully solved by single-crystal, X-ray crystallography. Aspects of the molecular and crystal structures of the complexes are shown in Figures 2–10 and S8–S11. Numerical data are listed in Tables 1–4 and S1–S4. Complexes **4**·MeCN_Eu, **7**·MeCN_Dy, and **10**·MeCN_Yb are isomorphous. Thus, only the molecular and crystal structure of **7**·MeCN_Dy will be described in detail. Complexes **17**_Tb and **18**_Dy are also isomorphous and only the molecular and crystal structure of compound **18**_Dy will be discussed in detail.

**Table 1.** Selected bond distances (Å) and angles (°) for complexes **4**·MeCN_Eu, **7**·MeCN_Dy, and **10**·MeCN_Yb [a].

Bond Distances (Å)	4·MeCN_Eu [b]	7·MeCN_Dy [c]	10·MeCN_Yb [d]
Ln-O1	2.310(1)	2.264(3)	2.224(1)
Ln-O2	2.300(1)	2.262(3)	2.218(1)
Ln-O1W	2.403(2)	2.366(3)	2.312(2)
Ln-O3	2.511(1)	2.479(3)	2.452(1)
Ln-O4	2.480(1)	2.439(3)	2.399(1)
Ln-O6	2.572(1)	2.548(3)	2.526(1)
Ln-O8	2.536(1)	2.491(2)	2.445(1)
C1-C6	1.431(2)	1.441(5)	1.435(3)
C6-C7	1.417(2)	1.415(6)	1.419(3)
C7-N1	1.298(2)	1.299(6)	1.294(3)
C1-O1	1.302(2)	1.302(5)	1.302(2)
C14-C19	1.428(3)	1.433(5)	1.433(3)
C19-C20	1.419(3)	1.414(6)	1.420(3)
C20-N2	1.307(2)	1.304(6)	1.304(3)
C14-O2	1.309(2)	1.311(5)	1.305(2)

Table 1. *Cont.*

Bond Distances (Å)	4·MeCN_Eu [b]	7·MeCN_Dy [c]	10·MeCN_Yb [d]
Bond angles (°)			
O1-Ln-O2	77.6(1)	77.8(1)	78.0(1)
O1W-Ln-O1	79.8(1)	79.7(1)	79.6(1)
O1W-Ln-O2	87.8(1)	87.6(1)	87.3(1)
O3-Ln-O4	51.3(1)	51.9(1)	52.7(1)
O3-Ln-O6	114.7(1)	115.0(1)	115.5(1)
O8-Ln-O2	153.5(1)	152.7(1)	152.2(1)
O11-Ln-O1	147.8(1)	147.1(1)	147.1(1)

[a] The same atom numbering scheme is applied for the three complexes: [b] Ln = Eu, [c] Ln = Dy, [d] Ln = Yb.

The crystal structure of **7**·MeCN_Dy consists of complex molecules [Dy(NO$_3$)$_3$(salanH)$_2$(H$_2$O)] and lattice MeCN molecules. Their ratio in the crystal is 1:1. The coordination sphere of the Dy^{III} centeris composed of three bidentate chelating nitrato groups and two oxygen atoms that belong to two organic ligands and one oxygen atom from the aquo ligand (Figure 2). Thus, the metal ions is 9-coordinate. The salanH molecules behave as monodentate O-donor ligands. The acidic hydrogen atom of each neutral ligand is clearly located on the nitrogen atom of the Schiff-base linkage and the ligands are, thus, in their zwitterionic form (Scheme 3). The protonation of the nitrogen atom blocks the second possible coordination site of salanH. It should be mentioned at this point that the acidic hydrogen atom is located on the oxygen atom in the crystal structures of the various polymorphs of the free ligand [75–78]. There are two intramolecular H bonds of moderate strength in the complex molecule with the protonated nitrogen atoms N1 and N2 being the donors and the negatively charged coordinated oxygen atoms O1 and O2 being the acceptors, respectively (Figure S8). Their dimensions are: N1-H(N1) 0.91(4) Å, H(N1)···O1 1.84(5) Å, N1···O1 2.609(4) Å, N1-H(N1)···O1 140(4)°, and N2-H(N2) 0.70(4) Å, H(N2)···O2 2.10(4) Å, N2···O2 2.676(5) Å, N2-H(N2)···O2 140(5)°. Each [Dy(NO$_3$)$_3$(salanH)$_2$(H$_2$O)] molecule is also H-bonded to a lattice MeCN molecule. The donor is the oxygen atom of the coordinated H$_2$O molecule and the acceptor is the nitrogen atom. The dimensions of this H bond are: H$_B$(O1W)···N6 2.16(6) Å, O1W···N6 2.836(7) Å, and O1W-H$_B$(O1W)···N6 169(7)°.
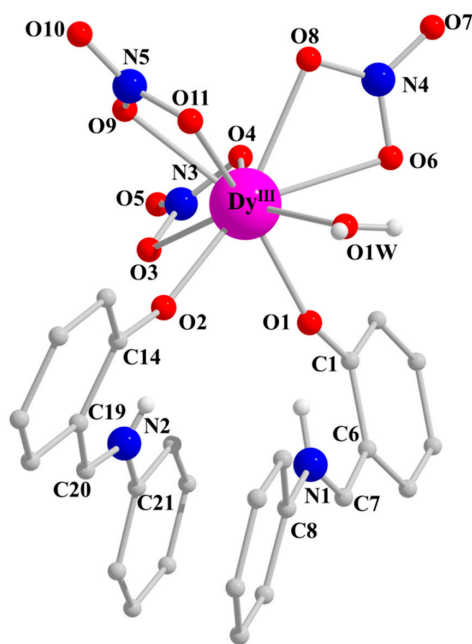

Figure 2. Partially labelled plot of the structure of the molecule [Dy(NO$_3$)$_3$(salanH)$_2$(H$_2$O)] that is present in the crystal structure of complex **7**·MeCN_Dy.
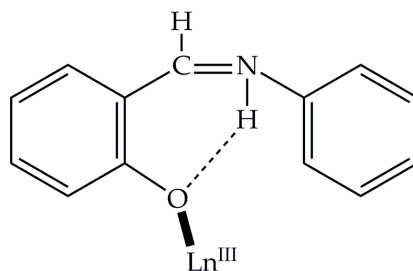
Scheme 3. The coordination mode of the zwitterionic ligand salanH in the mononuclear complexes of the present work. The coordination bond is drawn in bold.

The Dy-O bond lengths fall in the range of 2.300(1)–2.572(1) Å and are typical for 9-coordinate Dy(III) complexes [51,55,57]. The bond lengths of Dy^{III} to deprotonated phenoxido oxygens [2.300(1) and 2.310(1) Å] are shorter than the distances to the nitrato and aquo oxygens. Each Ln-O bond distance in the three isomorphous complexes **4·MeCN_Eu**, **7·MeCN_Dy**, and **10·MeCN_Yb** follows the order $Yb^{III} < Dy^{III} < Eu^{III}$, which is a consequence of the well-known trend of lanthanide contraction. The C1-O1/C14-O2 [1.302(5), 1.311(5) Å], C6-C7/C19-C20 [1.415(6), 1.414(6) Å], and C7-N1/C20-N2 [1.299(6), 1.304(6) Å] bond lengths in the salanH ligands of **7·MeCN_Dy** (as well as in **4·MeCN_Eu** and **10·MeCN_Yb**) indicate their enolate-protonated imine character (Scheme 3). However, the fact that these bond lengths are shorter, shorter, and longer, respectively, than those of the various polymorphic forms of salanH (the corresponding distances in the free ligand are ~1.35, 1.45–1.53, and ~1.27 Å) might suggest a small degree of ketone-amine character in the bonding scheme of the coordinated organic ligands. It is proposed that **7·MeCN_Dy** has their ligands in an intermediate structure between phenolate and quinoid tautomers with a higher percentage of the former and does not, therefore, exist in either two limiting structural forms. This proposal is further supported by the fact that the C1-C6 and C14-C19 distances [1.441(5) and 1.433(5) Å in **7·MeCN_Dy**] are slightly longer than the other carbon-carbon distances in the corresponding benzylidene rings of coordinated salanH ligands [1.363(7)–1.410(7) and 1.361(7)–1.410(6) Å, respectively].

There are no Archimedean, Platonic, and Catalan polyhedra with nine vertices and also no prisms or antiprisms can be constructed with this number of vertices. Thus, the only shapes that may be considered are those listed in Table S1. Using the program SHAPE [82], the best fit obtained for the Ln^{III} centers in **4·MeCN_Eu**, **7·MeCN_Dy**, and **10·MeCN_Yb** is for the spherical tricapped trigonal prism (Figure 3, Table S1) with the nitrato atoms O3, O6, and O11 being the spherically distributed capping atoms. Since the nitrato coordinated groups impose small bite angles (~51°), the polyhedra are distorted.
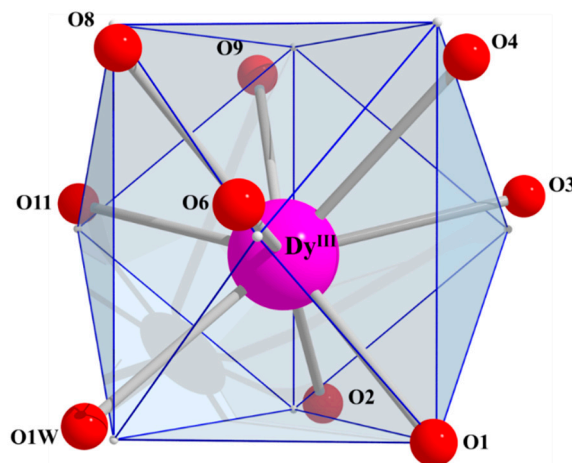
Figure 3. The spherical tricapped trigonal prismatic coordination polyhedron of the Dy^{III} center in complex **7·MeCN_Dy**. The smaller cream spheres define the vertices of the ideal polyhedron.
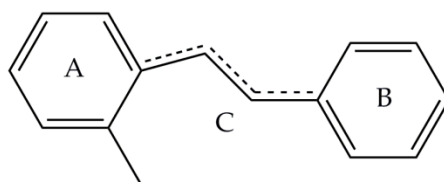
The two coordinated salanH ligands in the three complexes deviate from planarity. The ligand bearing N2 is more planar than the ligand bearing N1 (Table 2, Scheme 4). For example, in complex **7**·MeCN_Dy, the angle φ between the aromatic rings of the ligand possessing N2 is 11.5° while the angle between the rings of the ligand possessing N1 is 28.9°.

Table 2. Diagnostic angles (°) between planes of coordinated salanH in complexes **4**·MeCN_Eu, **7**·MeCN_Dy, and **10**·MeCN_Yb [a].

Angles (°)	4·MeCN_Eu	7·MeCN_Dy	10·MeCN_Yb
φ(A,B)	28.7 [b], 11.1 [c]	28.9 [b], 11.5 [c]	28.8 [b], 11.8 [c]
ψ(A,C)	4.8 [b], 3.5 [c]	5.3 [b], 3.4 [c]	5.2 [b], 3.4 [c]
ω(B,C)	24.4 [b], 7.7 [c]	24.2 [b], 8.1 [c]	24.1 [b], 8.5 [c]

[a] For the general definition of planes A, B, and C, see Scheme 4. [b] These values refer to the planes C1C2C3C4C5C6 (plane A), C8C9C10C11C12C13 (plane B), and C6C7N1C8 (plane C), see Figure 2. [c] These values refer to the planes C14C15C16C17C18C19 (plane A), C21C22C23C24C25C26 (plane B), and C19C20N2C21 (plane C), see Figure 2.

Scheme 4. Definition of the planes A, B, and C in the coordinated salanH ligands in complexes **4**·MeCN_Eu, **7**·MeCN_Dy, **10**·MeCN_Yb, **17**_Tb and **18**_Dy, and in the lattice salanH molecule in **17**_Tb and **18**_Dy.

Complexes **4**·MeCN_Eu, **7**·MeCN_Dy and **10**·MeCN_Yb have a similar formula with complexes [Ln(NO$_3$)$_3$(5BrsalanH)$_2$(H$_2$O)]·MeCN where Ln = Pr, Sm, Gd, Dy, Er [57] with analogous coordination modes for the ligands involved. However, they exhibit structural differences with the three main ones being: (i) The complexes of the present work have no molecular symmetry elements while the Ln(III)/5BrsalanH complexes possess a mirror plane symmetry. (ii) The two salanH ligands are in "*syn*" or ("*cis*") positions in **4**·MeCN_Eu, **7**·MeCN_Dy, and **10**·MeCN_Yb [the O1-Ln^{III}-O2 angle is in the 77.6(1)–78.0(1)° range] while the 5BrsalanH ligands are in "*anti*" (or "*trans*") positions [the corresponding O1-Ln^{III}-O1' angle is in the 162.5(1)–165.4(1)° range] and (iii) The coordination polyhedra of the Ln^{III} ions are spherically tricapped trigonal prisms in **4**·MeCN_Eu, **7**·MeCN_Dy, and **10**·MeCN_Yb, but spherical capped square antiprisms in the 5BrsalanH complexes.

The crystal structure of **18**_Dy contains complex molecules [Dy(NO$_3$)$_3$(salanH)$_2$(MeOH)] (Figure 4) and lattice salanH molecules (Figure 5) in a 1:1 ratio. The Dy^{III} ion is a 9-coordinate and is bound to six oxygen atoms from the three bidentate chelating nitrato groups to the oxygen atom from the terminally coordinated MeOH molecule and to two oxygen atoms that belong to the zwitterionic monodentate salanH ligands (Scheme 3). There are three classical intramolecular H bonds of medium strength within the complex. The donors are the protonated nitrogen atoms of the salanH ligands (N1, N2) and the acceptors are the coordinated phenoxido atoms O1 and O2 and the coordinated nitrato oxygen atom O6. Their dimensions are: N1-O1 2.667(4) Å, H(N1)···O1 1.96(5) Å, N1-H(N1)···O1 135(4)°; N1-O6 3.156(4) Å, H(N1)···O6 2.50(5) Å, N1-H(N1)···O6 131(4)°; N2-O2 2.640(4) Å, H(N2)···O2 1.90(5) Å, and N2-H(N2)···O2 139(5)°. The lattice (i.e., uncoordinated) salanH molecule is also in its zwitterionic form. A strong intramolecular H bond exists in the lattice molecule. Its dimensions are: N6-O13 2.504(4) Å, H(N6)···O13 1.76(4) Å, and N6-H(N6)···O13 141(5)°.

Table 3. Selected bond distances (Å) and angles (°) for complexes 17_Tb and 18_Dy [a].

Bond Distances (Å)	17_Tb [d]	18_Dy [e]
Ln-O1	2.304(3)	2.292(2)
Ln-O2	2.307(3)	2.296(2)
Ln-O12 [b]	2.365(4)	2.361(3)
Ln-O3	2.491(4)	2.482(3)
Ln-O4	2.475(4)	2.461(3)
Ln-O6	2.434(4)	2.420(3)
Ln-O8	2.475(5)	2.469(3)
Ln-O9	2.528(4)	2.520(3)
Ln-O10	2.460(4)	2.444(2)
C1-C6	1.436(7)	1.437(5)
C6-C7	1.415(8)	1.414(6)
C7-N1	1.296(7)	1.304(5)
C1-O1	1.306(6)	1.307(4)
C14-C19	1.435(7)	1.431(5)
C19-C20	1.420(8)	1.421(5)
C20-N2	1.298(7)	1.295(5)
C14-O2	1.297(6)	1.304(4)
C28 [c]-C33 [c]	1.411(5)	1.427(6)
C33 [c]-C34 [c]	1.414(8)	1.416(5)
C34 [c]-N6 [c]	1.307(7)	1.305(5)
C28 [c]-O13 [c]	1.308(6)	1.303(5)
Bond angles (°)		
O1-Ln-O2	151.1(1)	150.9(1)
O12 [b]-Ln-O1	87.0(1)	87.2(1)
O12 [b]-Ln-O2	87.2(1)	87.1(1)
O3-Ln-O4	51.4(1)	51.6(1)
O3-Ln-O6	73.6(1)	73.6(1)
O8-Ln-O2	72.0(1)	71.9(1)
O10-Ln-O1	79.5(1)	79.2(1)

[a] The same atom numbering scheme is applied for the two complexes. [b] This atom belongs to the coordinated MeOH molecule. [c] These atoms belong to the lattice (i.e., non-coordinated) salanH molecule, see Figure 5. [d] Ln = Tb. [e] Ln = Dy.
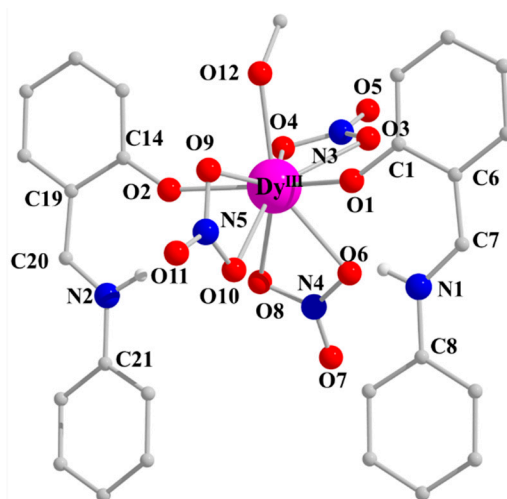

Figure 4. Partially labelled plot of the structure of the molecule [Dy(NO$_3$)$_3$(salanH)$_2$(MeOH)] that is present in the crystal structure of complex **18_Dy**.
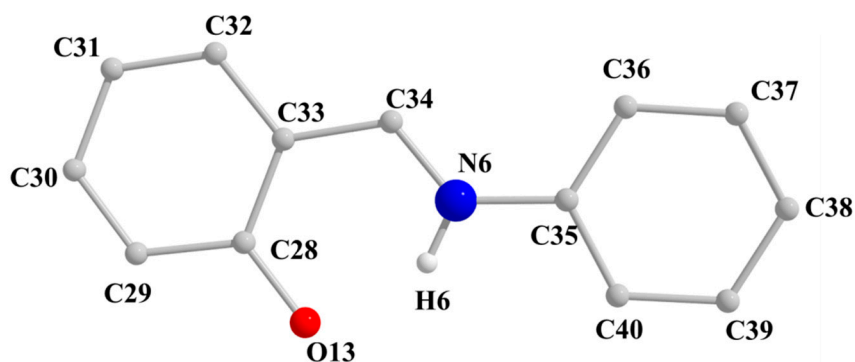
Figure 5. Fully labeled plot of the structure of the lattice free salanH molecule that is present in the crystal structure of complex **18_Dy**.

The Dy-O bond distances are in the range 2.304(3) to 2.528(4) Å. The deprotonated oxygen atoms of salanH are closer to the Dy^{III} center than the oxygen atoms of the nitrato and MeOH ligands. The C1-O1/C14-O2 [1.307(4), 1.304(4) Å], C6-C7/C19-C20 [1.414(6), 1.421(5) Å], and C7-N1/C20-N2 [1.304(5), 1.295(5) Å] bond lengths of the salanH ligands in **18_Dy** (as well as in **17_Tb**) indicate their enolate-protonated imine character (Scheme 3). As in the case of **4·MeCN_Eu**, **7·MeCN_Dy** and **10·MeCN_Yb**, these bond lengths are shorter, shorter, and longer, respectively, than those of the various polymorphic forms of salanH and this might suggest a small degree of a ketone-amine character in the bonding scheme of the coordinated salanH ligands. The corresponding C28-O13 [1.303(5) Å], C33-C34 [1.416(5) Å], and C34-N6 [1.305(5) Å] bond distances reveal the same trend for the lattice salanH molecule.

The coordination polyhedra of the Ln^{III} centers in **17_Tb** and **18_Dy** can be best described as spherical capped square antiprisms with the nitrato oxygen O9 being the capping atom (Figure 6, Table S2).
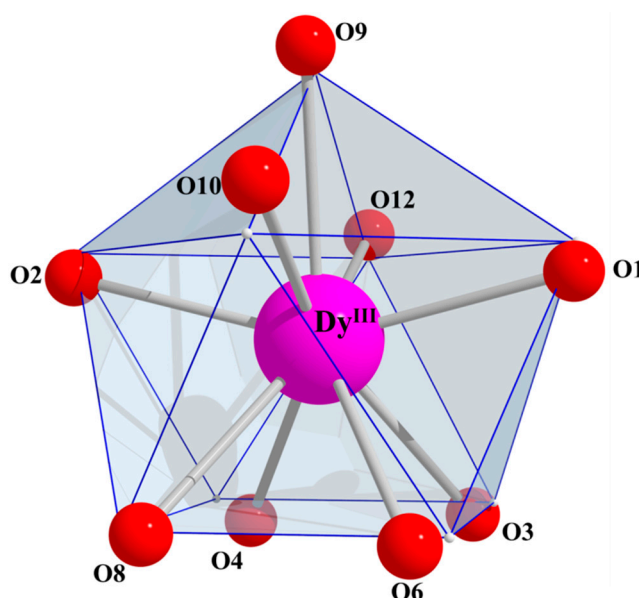
Figure 6. The spherical capped square anti-prismatic coordination polyhedron of the Dy^{III} center in complex **18_Dy**. The smaller cream spheres define the vertices of the ideal polyhedron.

One of the two salanH ligands in **17_Tb** and **18_Dy** is almost planar. The angle between the two aromatic rings is 1.1° in **17_Tb** and 1.0° in **18_Dy**. The second salanH ligand is somewhat less planar with the angle being 9.6° in **17_Tb** and 9.8° in **18_Dy**. The lattice salanH molecule is nearly planar and the angle is 2.4° for both complexes.

By contrast with **4**·MeCN_Eu, **7**·MeCN_Dy and **10**·MeCN_Yb, the salanH ligands in **17**_Tb and **18**_Dy are in mutually "*anti*" or "*trans*" positions with the O1-Ln-O2 angle [151.1(1)° in **17**_Tb and 150.9(1)° in **18**_Dy] being the largest donor atom-Ln^{III}-donor atom bond angle in the coordination sphere. In respect of this, the conformation of **17**_Tb and **18**_Dy resembles that of complexes [Ln(NO$_3$)$_3$(5BrsalanH)$_2$(H$_2$O)]·MeCN (Ln = Pr, Sm, Gd, Dy, Er) [57].

Table 4. Diagnostic angles (°) between planes of coordinated and lattice salanH molecules in complexes **17**_Tb and **18**_Dy [a].

| Angles (°)	17_Tb	18_Dy
φ(A,B)	1.1 [b], 9.6 [c], 2.4 [d]	1.0 [b], 9.8 [c], 2.4 [d]
ψ(A,C)	1.2 [b], 2.6 [c], 1.0 [d]	0.9 [b], 2.0 [c], 1.1 [d]
ω(B,C)	1.6 [b], 11.4 [c], 1.8 [d]	0.9 [b], 11.0 [c], 1.7 [d]

[a] For the general definitions of planes A, B, and C, see Scheme 4. [b] These values refer to the planes C1C2C3C4C5C6 (plane A), C8C9C10C11C12C13 (plane B), and C6C7N1C8 (plane C), see Figure 4. [c] These values refer to the planes C14C15C16C17C18C19 (plane A), C21C22C23C24C25C26 (plane B), and C19C20N2C21 (plane C), see Figure 4. [d] These values refer to planes C28C29C30C31C32C33 (plane A), C35C36C37C38C39C40 (plane B), and C33C34N6C35 (plane C) of the lattice salanH molecules that are present in the two complexes, see Figure 5.

A variety of similar intermolecular interactions are present in the crystal packing of the isomorphous complexes **4**·MeCN_Eu, **7**·MeCN_Dy and **10**·MeCN_Yb. We discuss in this paper the interactions for complex **7**·MeCN_Dy. Centrosymmetrically-related entities [Dy(NO$_3$)$_3$(salanH)$_2$(H$_2$O)]·MeCN form dimers through the O1W···O6′ and O1W′···O6 H bonds (Figure S8; ′ = −*x* + 2, −*y*, −*z* − 1). The Dy···Dy′ distance within each dimer is 6.588(4) Å [the Eu···Eu′ distance in **4**·MeCN_Eu is 6.623(1) Å and the Yb···Yb′ distance in **10**·MeCN_Yb is 6.562(1) Å]. Neighboring {[Dy(NO$_3$)$_3$(salanH)$_2$(H$_2$O)]·MeCN}$_2$ dimers interact further through π-π stacking interactions of the salanH aniline rings forming chains of dimers parallel to the [-101] crystallographic direction (Figure 7). The distance between the centrosymmetrically-related rings is 3.558(6) Å [this distance is 3.551(3) Å in **4**·MeCN_Eu and 3.560(3) Å in **10**·MeCN_Yb]. The shortest interdimer Dy···Dy distance along the chains is 9.586(1) Å [Eu···Eu = 9.628(1) Å, Yb···Yb = 9.549(1) Å]. The shortest inter-chain metal···metal distances are 8.056(1) (**7**·MeCN_Dy), 8.050(1) (**4**·MeCN_Eu), and 8.079(1) (**10**·MeCN_Yb) with neighboring chains linked through C13-H(C13)···O8‴ (*x* − 1, *y*, *z*) H-bonding interactions where C13 is an aromatic carbon atom of the benzylidene ring of one salanH ligand. The chains are also "bridged" by MeCN molecules through the H$_B$(O1W)···N6 (already mentioned) and C28-H$_B$(C28)···O4″ (*x*, *y* − 1, *z*) H-bonding interactions [the shortest metal···metal distance along this pathway is 11.696(1) Å for **7**·MeCN_Dy, 11.729(1) Å for **4**·MeCN_Eu and 11.657(1) Å for **10**·MeCN_Yb] forming the 3D architecture of the complexes (Figure S9). C28 is the methyl carbon atom of the lattice MeCN molecule. The parameters of the H bonds for the three complexes are listed in Table S3.
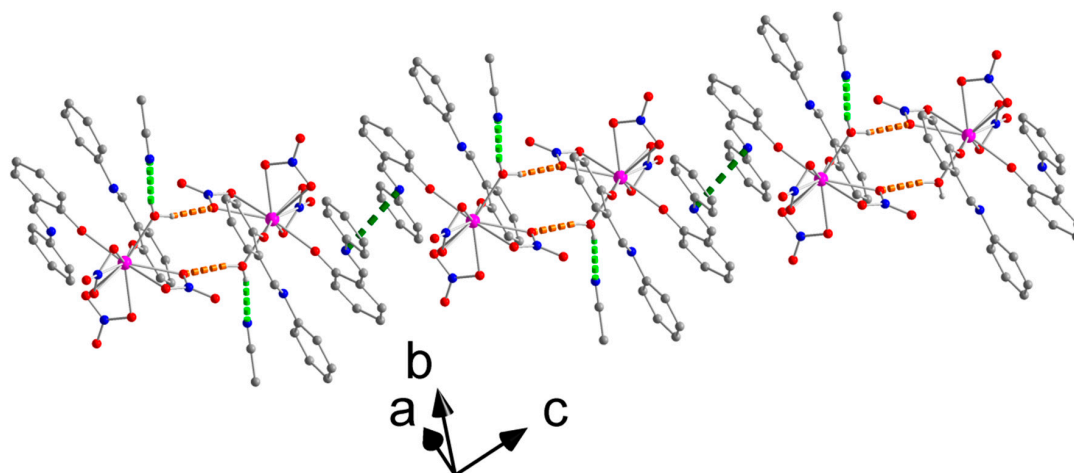
Figure 7. A portion of a chain of H-bonded dimers formed through π-π stacking interactions in the crystal structure of **7**·MeCN_Dy. The chain is parallel to the [-101] crystallographic direction. The π-π interactions are indicated by the dashed, dark green lines. The dashed, light green and orange lines represent the O1W-H$_B$(O1W)···N6 and O1W-H$_A$(O1W)···O6′ ($-x + 2$, $-y$, $-z - 1$) intermolecular H bonds, respectively.

The supramolecular features of the isomorphous complexes **17_Tb** and **18_Dy** are also interesting and we describe here those of the Dy(III) compound **18_Dy**. The H bonds within the [Dy(NO$_3$)$_3$(salanH)$_2$(MeOH)] complex molecule and the salanH lattice molecule have already been mentioned (see Figure S10). The lattice salanH molecules are H-bonded to the Dy^{III}-containing complex molecules through the C36-H(C36)···O11 and O12-H(O12)···O13 ($-x$, $-y + 2$, $-z + 2$) H bonds (Figure 8). In addition to H bonds, π-π stacking interactions also contribute to the supramolecular structure. There are two types of π-π interactions for each coordinated salanH molecule with neighboring salanH ligands, which is indicated with different colors in Figure 8 (dashed dark and light green). The salanH ligands whose interaction is indicated by the dashed dark green line form an angle of 5.3(1)° between their mean planes (the same value is found for **17_Tb**) and their centroid···centroid distance is 3.28 Å (3.27 Å for **17_Tb**). The salanH ligands whose interaction is indicated by the dashed light green line form an angle of 5.3(1)° between their mean planes for both 1**7_Tb** and **18_Dy** and their centroid···centroid distance is 3.41 Å for **18_Dy** and 3.36 Å for **17_Tb**. The complex molecules interact further via π-π stacking interactions through centrosymmetrically-related aniline rings (rings containing the C21, C22, C23, C24, C25, and C26 atoms) with the centroid···centroid distance being 3.36 Å for both compounds. All these different types of interactions result in a 3D architecture, which gives the characteristic of a hybrid molecular material to the complexes. In more detail, through the π-π interactions indicated by the light and green lines in Figure 8, a brick wall-type arrangement of the Dy^{III}-containing complex molecules is formed resulting in layers parallel to the (001) plane (Figure 9). The Dy^{III}···Dy^{III} distances within each layer are in the range 9.596(1)–10.298(1) Å [9.598(1)–10.312(1) Å for the Tb(III) complex]. The layers interact from one side with a centrosymmetrically-related layer of brick wall-type through π-π interactions involving the C21-containing aniline rings (Figure S11) and from the other side with a layer of lattice salanH molecules (Figure 10) parallel to the (001) plane through C36-H(C36)···O11 and O12-H(O12)···O13 ($-x$, $-y + 2$, $-z + 2$) H bonds (Figure 8). The layers are stacked along the c axis in such a way that two brick wall-type layers of the complex molecules are separated by a single layer of lattice salanH molecules (Figure S11), which give characteristics of a coordination complex-organic molecule hybrid material to the structures of 1**7_Tb** and **18_Dy**. In each layer of lattice salanH molecules, two types of overlap are observed with both relating molecules through a center of symmetry and their mean planes are at distances of 3.23(2) and 3.42(2) Å [3.27(4) and 3.41(4) Å for 1**7_Tb**] for the interactions indicated with dashed light violet-orange and mauve lines, respectively (Figure 10). The parameters of the H bonds for 1**7_Tb** and **18_Dy** are listed in Table S4.
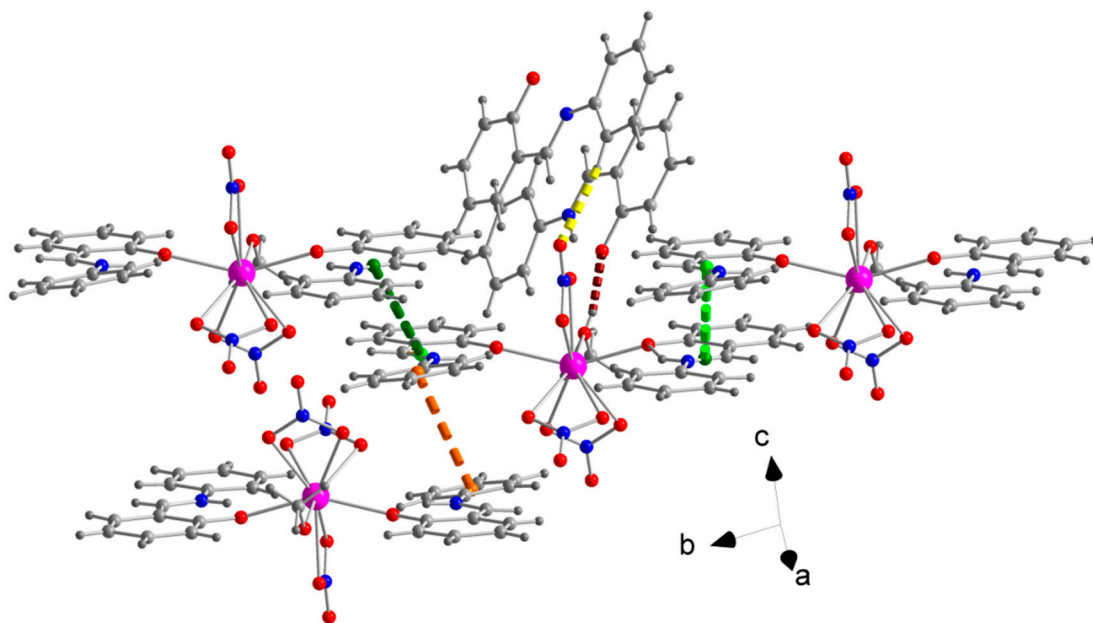
Figure 8. Different types of intermolecular interactions in the crystal structure of **18_Dy**. The dashed dark green and light green lines indicate the two types of π-π interactions between coordinated salanH ligands. The dashed orange lines indicate π-π stacking interactions between centrosymmetrically-related aniline rings of coordinated salanH ligands. The dashed yellow and dark red lines represent the C36-H(C36)···O11 and O12-H(O12)···O13 ($-x$, $-y + 2$, $-z + 2$) H bonds, respectively, which link the [Dy(NO$_3$)$_3$(salanH)$_2$(MeOH)] complex molecules and the lattice (i.e., non-coordinated) salanH molecules. Atom C36 is an aromatic carbon atom that belongs to the aniline ring of the lattice salanH molecule.
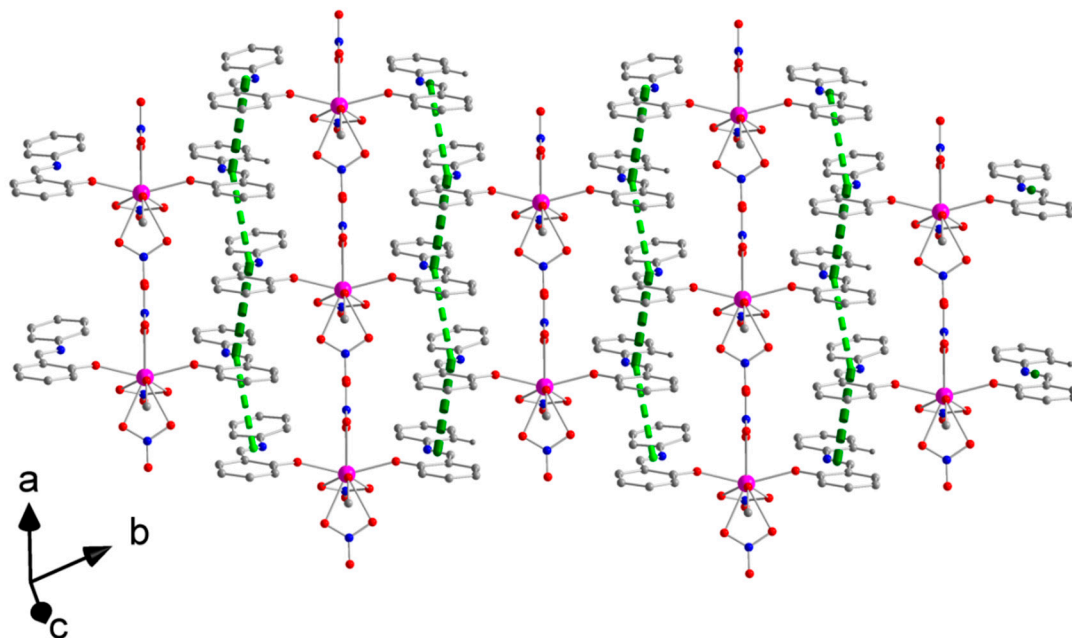
Figure 9. A brick wall-type layer of the [Dy(NO$_3$)$_3$(salanH)$_2$(MeOH)] molecules parallel to the (001) plane in the crystal structure of **18_Dy**. The dashed dark green and light green lines indicate the two types of intermolecular π-π interactions between coordinated salanH ligands.
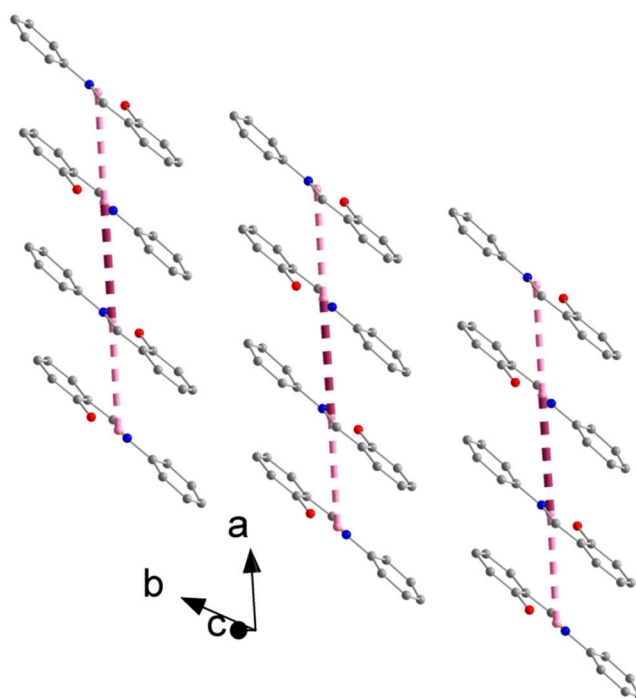
Figure 10. A layer of lattice salanH molecules parallel to the (001) plane in the crystal structure of **18_Dy**. The dashed light violet-orange and mauve lines indicate the two types of overlap.

2.4. Emission Studies

Solid-state, room-temperature photoluminescence studies have been performed for the free ligand salanH (Figure 11) and complexes **4·MeCN_Eu** (Figure 11), **5·MeCN_Gd** (Figure S12), **6·MeCN_Tb** (Figure S13), **7·MeCN_Dy** (Figure S14), **15_Eu** (Figure 11), **16_Gd** (Figure S15), **17_Tb** (Figure S16), and **18_Dy** (Figure S17).
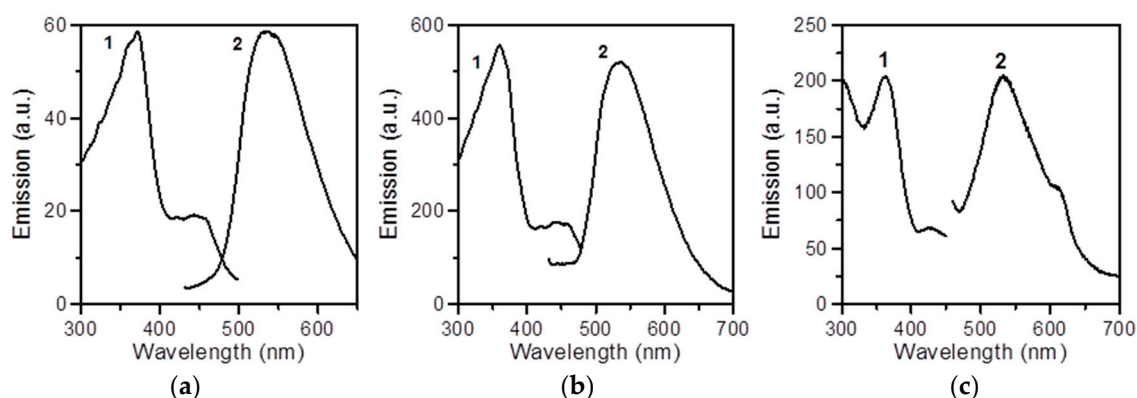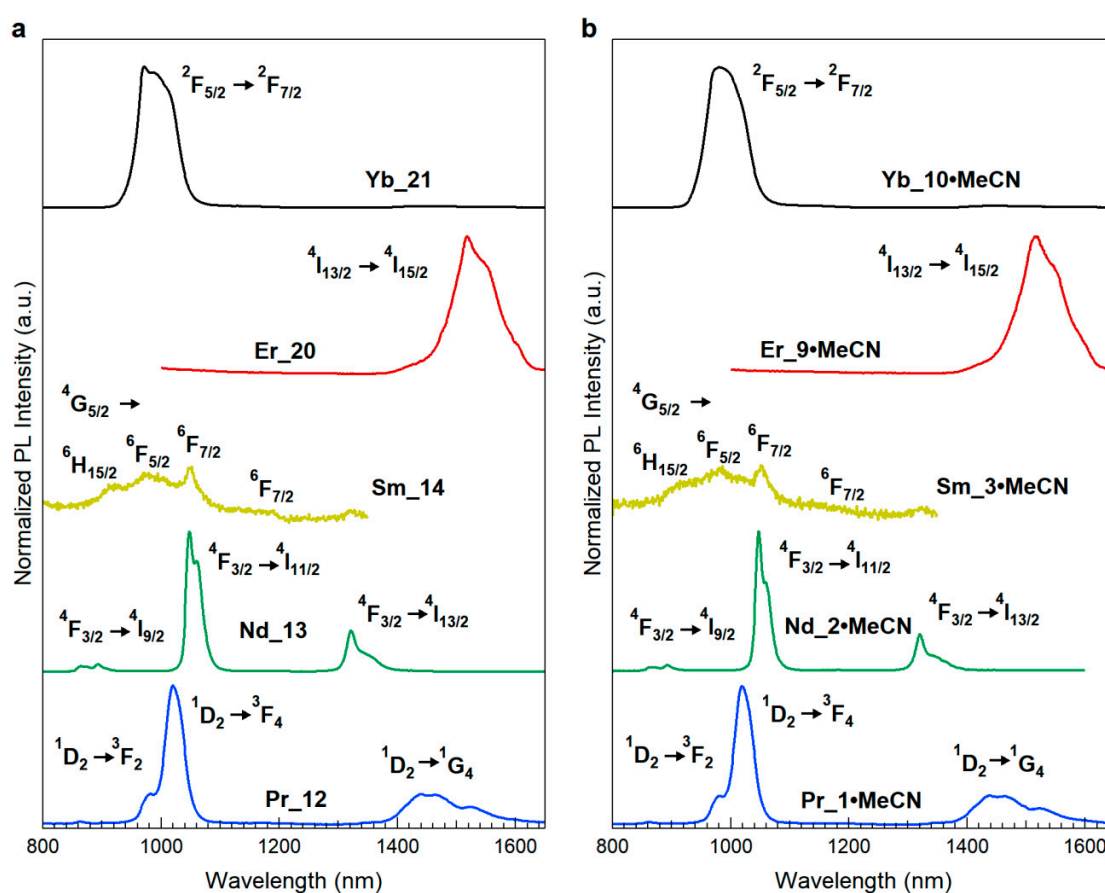

Figure 11. (**a**) Solid-state, room-temperature excitation (curve 1, maximum emission at 545 nm) and emission (curve 2, maximum excitation at 360 nm) spectra of free salanH, (**b**,**c**) Solid-state, room-temperature excitation (curve 1, maximum emission at 540 nm) and emission (curve 2, maximum excitation at 360 nm) spectra of complexes **4·MeCN_Eu** and **15_Eu**, respectively.

Upon maximum excitation at 360 nm, the free salanH ligand shows a broad emission with a maximum at 545 nm located in the green part of the visible spectrum.

The photoluminescence characteristics of the free ligand salanH and the Eu(III) (**4·MeCN_Eu**), Tb(III) (**6·MeCN_Tb**, **17_Tb**), and Dy(III) (**7·MeCN_Dy**, **18_Dy**) complexes are almost identical, which suggests no Ln^{III}-based emission. The same excitation and emission profiles are seen for solid **15_Eu** except an emission peak at 612 nm assigned [54,55] to the $^5D_0 \rightarrow ^7F_2$ transition and

indicates a partial sensitized red Eu^{III} emission. The photoluminescence characteristics of the Gd(III) complexes **5**·MeCN_Gd and **16**_Gd are nearly identical to those of the free salanH ligand and of complexes **4**·MeCN_Eu, **6**·MeCN_Tb, **7**·MeCN_Dy, and **17**_Tb and **18**_Dy. All these experimental facts indicate that the broad green emission at ~525 to 540 nm in the spectra of all the eight complexes is salanH-centered and, thus, the coordinated ligand cannot act as a "sensitizer" for 4f-metal luminescence. It seems that this Ln^{III}-independent emission is due to an efficient Ln^{III}-to-salanH back energy transfer [50,52,83]. A reason for this behavior might be the fact that the main absorption bands of coordinated salanH (at ~500 nm) are not close to the region where some Ln^{III} ions absorb (<400 nm) [57]. Upon the same excitation conditions, the room-temperature, solid-state emission spectra of the complexes are very similar with those recorded in acetone solutions (also at ~20 °C).

Solid-state, room temperature emission spectra upon CW laser excitation at 405 nm in the visible (Figure S18) and near-IR (Figure 12) regions have also been recorded for the Pr(III), Nd(III), Sm(III), Er(III), and Yb(III) complexes.

Figure 12. Solid-state, room-temperature near-IR emission spectra of complexes **1**·MeCN_Pr, **2**·MeCN_Nd, **3**·MeCN_Sm, **9**·MeCN_Er, and **10**·MeCN_Yb ((**b**), right) and **12**_Pr, **13**_Nd, **14**_Sm, **20**_Er, and **21**_Yb ((**a**), left).

The emission spectra in the visible region upon CW laser excitation at 405 nm are, in general, very similar with those of the Eu(III), Gd(III), Tb(III), and Dy(III) complexes mentioned above. Thus, they exhibit green, salanH-based luminescence. The similar f-f emission spectra of the Pr(III) complexes **1**·MeCN_Pr and **12**_Pr, exhibit, in addition to the broad band at ~540 nm, three weak peaks, a shoulder at ~580 nm assigned [41] to the $^3P_0 \rightarrow {}^3H_5$ transition, a rather broad peak at ~605 nm assigned to the $^1D_2 \rightarrow {}^3H_4$ transitions, and another shoulder assigned to the $^3P_0 \rightarrow {}^3F_2$ transition at ~615 nm. It, thus, seems that a partial energy transfer from the coordinated organic ligands to Pr^{III} is operative. The peak at ~605 nm is the most intense of the three due to the hypersensitivity of the $^1D_2 \rightarrow {}^3H_4$

transition [41]. As a rule, the Pr(III) complexes exhibit complicated emission spectra because the Pr^{3+} ion can display emission bands from three levels ($^3P_0$, $^1D_2$, and $^1G_4$) after exciting the absorption of organic ligands [84]. The Nd(III) complexes **2**·MeCN_Ndand **13**_Nd exhibit in addition to the broad salanH-based band at ~540 nm a weak emission feature with a fine structure at ~590 nm, which is difficult to assign.

The $T_1 \rightarrow S_0$ transition from the excited triplet state to the ground state of the organic ligand is generally disallowed at room temperature due to non-radiative losses. The non-radiative losses can be divided into intramolecular and external losses to the environment, which are mainly collisions with quenching sites (e.g., oxygen or water). At room temperature, even in the absence of oxygen and water, the non-radiative losses typically outclass the radiative transition and, thus, detection of the triplet state at room temperature is not possible [85,86].

The assignments of the near-IR emission bands for the Pr(III), Nd(III), Sm(III), Er(III), and Yb(III) complexes are located at the top of the corresponding peaks on Figure 12. For a given Ln^{III} ion, the emission spectra are very similar when displaying the characteristic lanthanide(III) emission peaks.

The emission spectra of the Pr(III) complexes **1**·MeCN_Pr and **12**_Pr show three bands at ~865, ~1020, and ~1465 nm, which can be assigned as originating from the $^1D_2 \rightarrow {}^3F_2$, $^1D_2 \rightarrow {}^3F_4$ and $^1D_2 \rightarrow {}^1G_4$ transitions, respectively [41,84]. Some crystal-field fine structures can be observed, which is an indication that the Pr^{III} center occupies well-defined crystallographic sites in the complex [84]. For the Nd(III) complexes **2**·MeCN_Nd and **13**_Nd, the spectra consist of three emission peaks that are assigned to the $^4F_{3/2} \rightarrow {}^4I_{9/2}$ (~885 nm), $^4F_{3/2} \rightarrow {}^4I_{11/2}$ (~1050 nm), and $^4F_{3/2} \rightarrow {}^4I_{13/2}$ (~1330 nm) transitions [40,41,43,84]. Among the three peaks, the $^4F_{3/2} \rightarrow {}^4I_{11/2}$ transition has the highest intensity with a potential in laser systems while the transition at ~1330 nm offers the opportunity to develop new materials suitable for an optical amplifier operating at 1.3 μm, which is one of the telecommunication windows [84]. For the near-IR emission spectra of the Sm(III) complexes **3**·MeCN_Sm and **14**_Sm, all the peaks come from the $^4G_{5/2}$ excited state [84]. In the case of the Er(III) complexes **9**·MeCN_Er and **20**_Er, the emission spectra display a peak at ~1530 nm, which covers a large spectral range from 1480 to 1620 nm. This is attributed to the typical $^4I_{13/2} \rightarrow {}^4I_{15/2}$ transition of Er^{III} [40,41,43,84]. There are a number of excited states of Er(III) from which emission is possible. The fact that emission is observed only from the $^4I_{13/2}$ state suggests that an efficient non-radiative decay pathway exists from those states to the $^4I_{13/2}$ state. The Er(III) complexes are promising for application in amplification because the transition at around 1530 nm is in the right position for the third telecommunication window [41,84]. To make possible a wide-gain bandwidth for optical amplification, a broad emission band is desirable. In our complexes, this requirement is realized since the full width at half-maximum is large (>60 nm). The Yb^{3+} ion is an unusual case in the Ln(III) emission because it has only one singlet excited state, $^2F_{5/2}$, and 10,200 cm^{-1} above the ground $^2F_{7/2}$ state [84]. The emission spectra of the Yb(III) complexes **10**·MeCN_Yb and **21**_Yb consist of the characteristic peak at ~990 nm, which is assigned to the $^2F_{5/2} \rightarrow {}^2F_{7/2}$ transition [41,84,87]. For **21**_Yb, the typical broader vibronic components at longer wavelengths are observed [84]. The near-IR emission of Yb(III) is very important because biological issues and fluids (e.g., blood) are relatively transparent in this region (around 1000 nm) and the development of Yb(III) complexes for various analytical and chemo sensor application is a "hot" research topic in medicinal inorganic chemistry.

The detailed elucidation of the mechanism of the near-IR emission properties of the Pr(III), Nd(III), Sm(III), Er(III), and Yb(III) complexes described in this work is beyond the scope of the present paper. With limited data at hand, the question asking if there is effective energy transfer from the triplet state of the salanH ligand to the near-IR emissive levels of the Ln^{III} ions is difficult to answer. We believe that there is no efficient energy transfer from the ligand for two reasons: (a) The strong excitation intensity (from the CW laser) is able to activate the Ln^{III}s emission levels and (b) the presence of the ligand-based green emission of the complexes in the spectra (Figure S18) at room temperature is indicative of an incomplete or zero energy transfer to the excited levels of the Ln^{III} ions [42].

2.5. Magnetic Studies of the Tb(III) and Dy(III) Complexes

The direct current (dc) magnetic susceptibility data (χ_M) on well dried samples of **6_Tb**, **7_Dy**, **17_Tb**, and **18_Dy** collected in the temperature (*T*) range 2.0 to 300 K under an applied field of 0.03 T are typical of mononuclear Tb(III) and Dy(III) complexes and will not be further discussed in detail. For example, the 298 K $\chi_M T$ values for **7_Dy** and **18_Dy** are ~14.3 cm^3·K·mol^{-1}, which is in very good agreement with the expected value for one Dy^{III} center ($^6H_{15/2}$, free ion, $S = 5/2$, $g_j = 4/3$). Upon cooling, the values of the $\chi_M T$ product decrease continuously and slowly reach the ~70% of their room-temperatures values at 2.0 K with the decrease being primarily due to the depopulation of the m_j sublevels of the ground *J* state [5]. The magnetization plots show a rapid increase at low fields and almost saturated values over 2 T (Figures S19 and S20). The magnetization values at the maximum applied field of 5 T (~6.5 $N\mu_B$) are significantly lower than the expected value for one isolate Dy^{III} center (10 $N\mu_B$), which can be attributed to the crystal-field effects that lead to a substantial magnetic anisotropy [5]. The observed experimental value is typical of mononuclear Dy(III) complexes [57].

Alternating current (ac) magnetic susceptibility experiments were carried out using a 4.0 G ac field oscillating in the frequency range of 10 to 1488 Hz in order to explore the magnetization dynamics of the four complexes. In the zero dc field, no out-of-phase (imaginary) components of the ac susceptibility, χ''_M, were detected for frequencies between 10 and 1488 Hz even at the lowest investigated temperature (2 K). Under an external dc field of 0.1 T (in order to suppress the QTM and to enhance the slow magnetic relaxation properties), well-defined, temperature-dependent and frequency-dependent χ''_M maxima were observed for the Dy(III) complexes **7_Dy** and **18_Dy** (Figure 13a,b), which indicated a field-induced slow magnetic relaxation. Complex **17_Dy** shows tails of peaks at low frequencies under an external static field of 0.15 T and a well-defined maximum was clearly visible only for the higher frequency examined (1488 Hz) (Figure 13c). The optimum dc fields were decided by examining the χ''_M vs. *T* response under different dc fields between 500 and 2000 G at two different ac frequencies (10 and 1000 Hz). A field-induced dependence of the susceptibility on temperature and frequency was observed and the optimum dc field that gives the clearest signal was selected for the ac measurements (Figure S21). For the Tb(III) complex **6_Tb**, no field-induced properties were observed.

While complex **7_Dy** presents a single set of maxima in the χ''_M vs. *T* graph in the 3.5–2.0 K range (2.0 K is the lowest temperature limit of our instrument), complex **18_Dy** presents the set of maxima at a higher temperature range (8–4 K) indicating better properties for the latter. Such a difference is also clear for the two Tb(III) complexes **6_Tb** and **17_Tb**. Complex **6_Tb** has no magnetic response at all while **17_Tb** shows χ''_M dependence upon *T*. For a given Ln^{III} center, the different magnetic response between the two complexes (**7_Dy** and **18_Dy** and **6_Tb** and **17_Tb**) is a consequence of the different crystal fields around the metal ion in the two families [5,6,10,15–33]. The different crystal fields arise mainly from the (i) different coordination geometries around the Ln^{III} centers (tricapped trigonal prismatic in **6_Tb** and **7_Dy** vs. capped square anti-prismatic in **17_Tb** and **18_Dy**), (ii) different coordinated solvent molecules (H$_2$O in **6_Tb** and **7_Dy** vs. MeOH in **17_Tb** and **18_Dy**), and (iii) the "*cis*" disposition of the salanH ligands in **6_Tb** and **7_Dy** as opposed to the "*trans*" disposition of the ligands in **17_Tb** and **18_Dy** (*vide supra*). Upon a more detailed examination, the better field-induced magnetic relaxation properties of **18_Dy** compared with those of **7_Dy** (a higher temperature range for the χ''_M maxima in the former than in the latter) and of **17_Tb** compared with those of **6_Tb** (appearance of signals in the former and no magnetic response in the latter) can be correlated with the supramolecular structures of the two families (*vide supra*). The presence of the lattice (i.e., uncoordinated) salanH molecules in **17_Tb** and **18_Dy** "dilutes," in a sense, these complexes (Figures 8–10, S10 and S11) resulting in longer Ln^{III}···Ln^{III} distances (>9.55 Å) and very diminished dipolar interactions between the Ln^{III} cations, which both lead to better SIM properties. On the other hand, the formation of the double H-bonded {[Ln(NO$_3$)$_3$(salanH)$_2$(H$_2$O)]·MeCN}$_2$ dimers (Figures 7 and S8) in the isomorphous complexes **6_Tb** and **7_Dy** results in a shorter (compared with **17_Tb** and **18_Dy**) intradimer Ln^{III}···Ln^{III} distance [6.588(4) Å in the case of the structurally characterized complex **7·MeCN_Dy**] and makes the complexes behave as "dinuclear" ones, which allows for very

weak antiferromagnetic Ln^{III}···Ln^{III} exchange interactions. The final result is the diminution (in **7_Dy**) or the disappearance (in **6_Tb**) of the field-induced, slow magnetic relaxation properties.
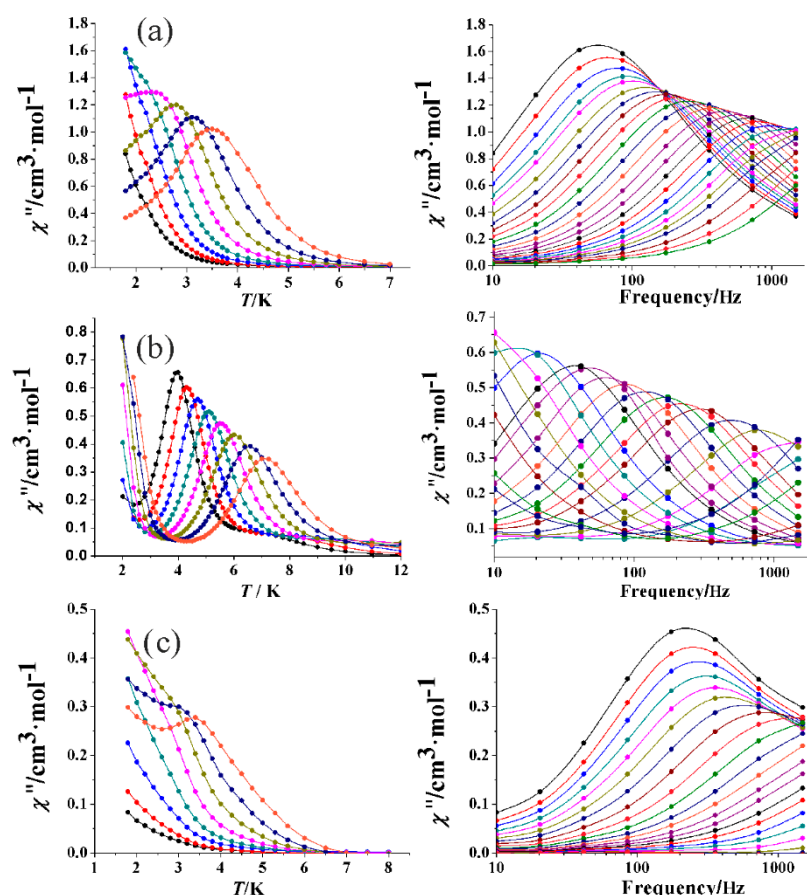
Figure 13. Out-of-phase ac molar magnetic susceptibility signals (χ'') vs. *T* (at different ac frequencies, left) and vs. ac frequency (at different low temperatures, right) for complexes (**a**) **7_Dy**, (**b**) **18_Dy**, and (**c**) **17_Tb**. All measurements were performed in the 10 to 1488 Hz frequency range under static field of 0.1 (**7_Dy**, **18_Dy**) and 0.15 T (**17_Tb**). Solid lines are guides for the eye.

The magnetic relaxation parameters of the Dy(III) complexes have been calculated using the Arrhenius Equation (3).

$$\ln(1/2\pi v) = \ln(1/\tau_0) - U_{eff}/K_B T \tag{3}$$

where τ_0 is the pre-exponential factor, K_B is the Boltzmann constant, and U_{eff} is the effective thermal energy barrier for magnetization reversal known as Orbach relaxation [88]. Best fits of the linear parts (Figure 14, left) give the parameters U_{eff} = 13.1 cm^{-1}, τ_0 = 4.5 × 10^{-7} s for **7_Dy**, and U_{eff} = 31.0 cm^{-1}, τ_0 = 2.5 × 10^{-7} s for **18_Dy**. Due to the lack of maxima in the χ''_M vs. *T* graph for **17_Tb**, a Debye relaxation has been assumed and the SIM parameters have been calculated using Equation (4) [89]. Considering a single relaxation process, the least-squares fits of the experimental data (Figure 14, center) give average values of U_{eff} = 14.8 cm^{-1}, τ_0 = 3.5 × 10^{-6} s. Due to a limited number of points in the Arrhenius plot for **7_Dy**, the Debye relaxation has been assumed and the SIM parameters have also been calculated using Equation (4) [89]. The parameters are U_{eff} = 15.9 cm^{-1}, τ_0 = 5.3 × 10^{-6} s (Figure 14, right) in a rather satisfactory agreement with the values obtained from the previous Arrhenius plot that involves only three points [86].

$$\ln(\chi''_M/\chi'_M) = \ln(v\tau_0) - U_{eff}/K_B T \tag{4}$$
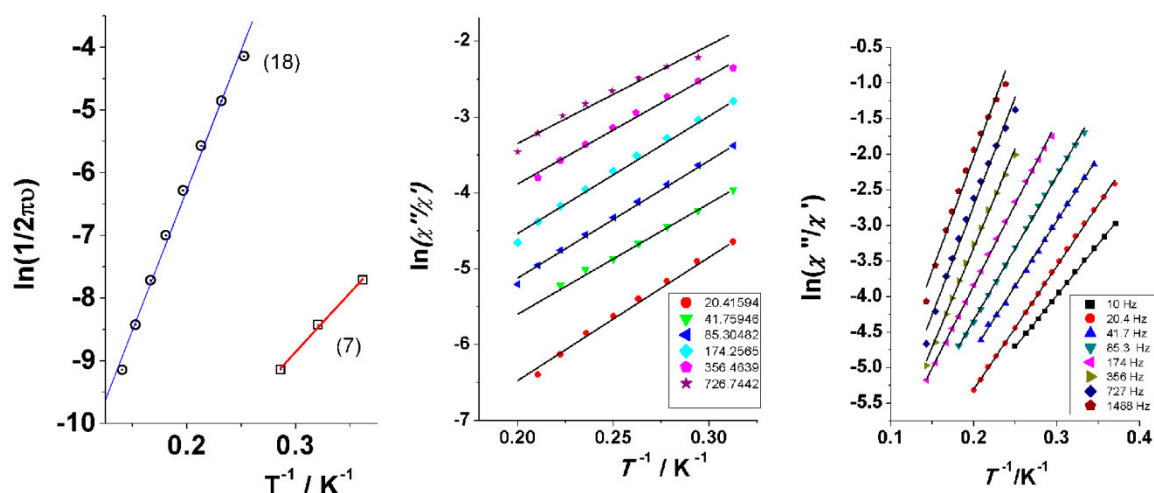
Figure 14. (**left**) Arrhenius plots for complexes **7_Dy** and **18_Dy** in applied dc fields of 0.1 T, (**center**) plots of $\ln(\chi''_{M}/\chi'_{M})$ vs. $1/T$ for **17_Tb** at different ac frequencies in an applied field of 0.15 T, and (**right**) plots of $\ln(\chi''_{M}/\chi'_{M})$ vs. $1/T$ for **7_Dy** at different ac frequencies in an applied field of 0.1 T. The solid lines represent the fits.

For complex **18_Dy**, an increase of the χ''_{M} values at low temperatures is clearly observable (Figure 13b, left), which suggests another set of maxima below 2 K. This second set might be also present in **7_Dy** and **17_Tb**, but the characteristics of our instrumental setup do not allow us to detect such a behavior below 2 K. The second set of maxima might indicate another pathway for magnetization relaxation different from the calculated Orbach process. This second set of maxima seems to be temperature-independent, which can be seen in the χ''_{M} vs. T graph for **18_Dy** (Figure 13b, left). Generally, such a temperature-independent process is attributed to a relaxation by fast QTM, but this seems to have been suppressed by the application of the external magnetic field.

The fit of the χ''_{M} vs. χ'_{M} data (Cole-Cole or Argand plot) for complexes **7_Dy** and **17_Tb** in the temperature range for which an Orbach process is assumed was performed using the CCfit software. The fit gives α values below 0.3 in both cases, which indicates a narrow distribution of the relaxation times (Figure S22, upper left and bottom left). A fit with reliable α values was not possible for **18_Dy** due to the simultaneous existence of two pathways for magnetization relaxation (Figure S22, upper right).

Due to the fact that, in the absence of high symmetry (as in **7·MeCN_Dy** and **18_Dy**), the Dy^{III} ground state is a doublet along the anisotropy axis with an angular momentum quantum number $m_j = \pm15/2$, we have determined the orientation of the ground-state magnetic anisotropy axes for the Dy^{III} centers in the two Dy(III) complexes by employing a method reported in 2013 [90]. The method is based on an electrostatic point charge approximation and requires only the knowledge of the single-crystal, X-ray structure of the complexes (and not the fitting of experimental magnetic data). In **7·MeCN_Dy** and **18_Dy**, the charge distribution consists of a plane containing the two phenoxido oxygen atoms and one bidentate nitrato group (**7·MeCN_Dy**) or one phenoxido oxygen atom and two bidentate nitrato groups (**18_Dy**). Following this method and using the FORTRAN program MAGELLAN [91], it is found that the ground-state magnetic anisotropy axis for the Dy^{III} center is directed towards one of the phenoxido oxygen atom in **7·MeCN_Dy** (Figure 15, right) and towards two nitrato groups in **18_Dy** (Figure 15, left). In our cases, the direction of the easy axes does not give valuable information and prediction since it is only a simple calculation. The distribution of the charged oxygen atoms (and the derived field) is spherical and any oblate-prolate [16] discussions are not possible.
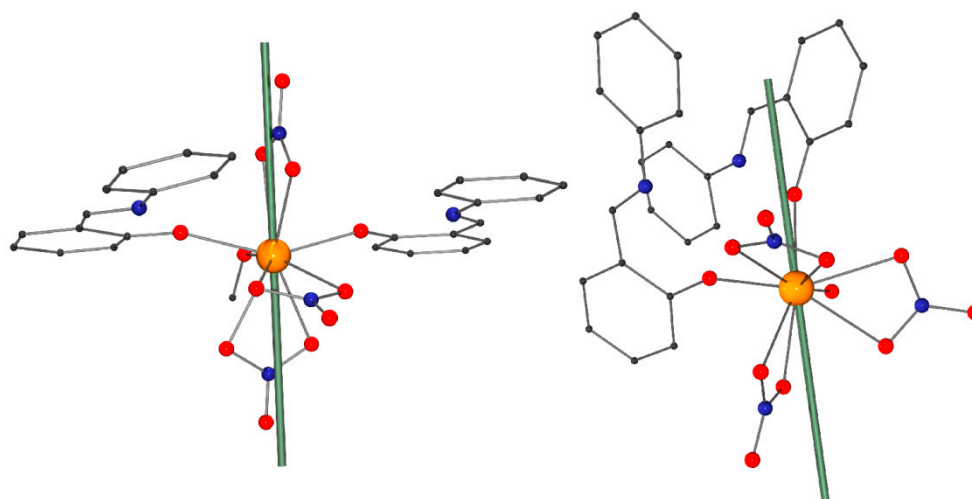
Figure 15. Ground-state magnetic anisotropy axes (green bars) for the Dy[III] centers in complexes **18_Dy** (**left**) and **7·MeCN_Dy** (**right**).

3. Experimental Section

3.1. Materials, Physical, and Spectroscopic Measurements

All manipulations were performed under aerobic conditions using reagents and solvents (Alfa Aesar, Karlsruhe, Germany; Aldrich, Tanfrichen, Germany) as received. The organic ligand salanH was synthesized in typical yields of >85%, as described in the literature [71]. Its purity was checked by microanalyses, IR and ^{1}H NMR spectra (Figure S6), and by the determination of its melting point (found, 46 °C, reported as 46 to 48 °C). Elemental analyses (C, H, N) were performed by the micro-analytical laboratory of the University of Patras (Patras, Greece). FT-IR spectra were recorded using a Perkin-Elmer 16PC spectrometer (Perkin-Elmer, Watham, MA, USA)with samples prepared as KBr pellets and as nujol or hexochlorobutadiene mulls. ^{1}H NMR spectra of the free ligand and the diamagnetic Y(III) complexes were recorded on a 400 MHz Bruker Avance DPX spectrometer (Bruker, Karlsruhe, Germany) using $(Me)_4Si$ as an internal standard. Powder X-ray diffraction (pXRDs) patterns were recorded on freshly prepared samples of the complexes with a Siemens D500 diffractometer (Siemens, Karlsruhe, Germany) using Cu Ka radiation. The measurements were performed using the following combination of slits: 1.0°/1.0°/1.0° as aperture diaphragms, 0.15° as a detector diaphragm, and 0.15° as a diffracted beam mono-chromator diaphragm. The measured 2θ range between 2° and 40° was scanned in steps of 0.03° per 3 s. The accelerating voltage and applied current were 40 KV and 35 mA, respectively. Diffuse reflectance spectra were obtained with an Agilent Cary 5000 instrument (Company Agilent Technologies, Santa Clara, CA, USA) in the 400 to 1600 nm by using an integrating sphere. A KBr reference pellet was prepared by grinding pure KBr (CAS Number 7758-02-3, Sigma Aldrich, Athens, Greece) >99% purity) in a pestle and mortar until a homogenous fine powder was obtained. This was then placed in a pellet-forming die under high pressure (approximately 8 tons) for about 5 min until a homogenous-looking disc was obtained. Individual discs of the samples of the complexes mixed and pressed with KBr (roughly 2% in KBr) were prepared in a similar manner. Solid-state, room-temperature emission and excitation spectra of selected complexes were recorded using a Cary Eclipse fluorescence spectrophotometer (Varian, Palo Alta, CA, USA). Solid-state, room-temperature photoluminescence measurements were performed using a Horiba Jobin Yvon iHR550 Fluorolog system (Horiba Jobin Yvon, Kyoto, Japan) coupled with a Hamamatsu RS5509-73liquid-nitrogen cooled photomultiplier. All the samples were encapsulated in a soda lime glass substrate and excited at 405 nm (70 mW) with a continuous-wave (CW) laser. Solil-state, variable-temperature and variable-field magnetic data for the Tb(III) and Dy(III) complexes were collected on powdered samples using a MPMS5 Quantum Design magnetometer (Quantum

Design, San Diego, CA, USA) operating at 0.03 T in the 300 to 2.0 K range for the magnetic susceptibility and at 2.0 K in the 0 to 5 T range for the magnetization measurements. Diamagnetic corrections were applied to the observed susceptibilities using Pascal's constants [92].

3.2. Synthesis of the Representative Complex [Dy(NO$_3$)$_3$(salanH)$_2$(H$_2$O)]·MeCN (**7**·MeCN_Dy)

To a stirred yellow solution of salanH (0.17 g, 0.1 mmol) in MeCN (5 mL) solid Dy(NO$_3$)$_3$·5H$_2$O (0.31 g, 0.1 mmol) was added. The solid soon dissolved and the resulting yellowish orange solution was stirred for a further 5 min and stored in a closed flask at room temperature. X-ray quality, orange crystals of the product were obtained within 24 h. The crystals were collected by filtration, washed with cold MeCN (1 mL) and Et$_2$O (2 × 2 mL), and dried in a vacuum dessicator overnight. The yield was 53% (based on the ligand available). The complex was satisfactorily analyzed as lattice MeCN-free, i.e., as **7**. Anal. calc. for C$_{26}$H$_{24}$N$_5$O$_{12}$Dy (found values in parentheses): C 41.03 (41.17), H 3.19 (3.24), N 9.20 (9.17) %. IR bands (KBr, cm^{-1}): 3396mb, 3068w, 1636s, 1610s, 1590m, 1536s, 1482sb, 1384m, 1318m, 1288s, 1240m, 1228m, 1182m, 1144s, 1122w, 1042sh, 1030m, 1010m, 906w, 872m, 832w, 812m, 788m, 754s, 688m, 584m, 554w, 518m, 502sh, 470w, 458w, and 410sh.

3.3. Syntheses of [Pr(NO$_3$)$_3$(salanH)$_2$(H$_2$O)]·MeCN (**1**·MeCN_Pr), [Nd(NO$_3$)$_3$(salanH)$_2$(H$_2$O)]·MeCN (**2**·MeCN_Nd), [Sm(NO$_3$)$_3$(salanH)$_2$(H$_2$O)]·MeCN (**3**·MeCN_Sm), [Eu(NO$_3$)$_3$(salanH)$_2$(H$_2$O)]·MeCN (**4**·MeCN_Eu), [Gd(NO$_3$)$_3$(salanH)$_2$(H$_2$O)]·MeCN (**5**·MeCN_Gd), [Tb(NO$_3$)$_3$(salanH)$_2$(H$_2$O)]·MeCN (**6**·MeCN_Tb), [Ho(NO$_3$)$_3$(salanH)$_2$(H$_2$O)]·MeCN (**8**·MeCN_Ho), [Er(NO$_3$)$_3$(salanH)$_2$(H$_2$O)]·MeCN (**9**·MeCN_Er), [Yb(NO$_3$)$_3$(salanH)$_2$(H$_2$O)]·MeCN (**10**·MeCN_Yb) and [Y(NO$_3$)$_3$(salanH)$_2$(H$_2$O)]·MeCN (**11**·MeCN_Y)

These complexes were prepared in an identical manner with **7**·MeCN_Dy by simply replacing Dy(NO$_3$)$_3$·5H$_2$O with the equivalent amount of the appropriate Ln(NO$_3$)$_3$·xH$_2$O starting material ($x = 5$ or 6). Typical yields were in the 50% to 60% range (based on salanH). The complexes were satisfactorily analyzed as lattice MeCN-free. In some samples, a small percentage of lattice MeCN (typically 0.1–0.4 moles per mole of the complex) could also fit well with the experimental microanalytical data. Anal. calc. for C$_{26}$H$_{24}$N$_5$O$_{12}$Ln (found values in parentheses): **1** (Ln = Pr): C 42.22 (42.66), H 3.28 (3.30), N 9.47 (9.60) %, **2** (Ln = Nd): C 42.04 (41.87), H 3.26 (3.35), N 9.43 (9.51) %, **3** (Ln = Sm): C 41.70 (41.91), H 3.24 (3.28), N 9.35 (9.47) %, **4** (Ln = Eu): C 41.61 (41.77), H 3.23 (3.17), N 9.33 (9.43) %, **5** (Ln = Gd): C 41.32 (41.17), H 3.21 (3.28), N 9.27 (9.42) %, **6** (Ln = Tb): C 41.22 (41.38), H 3.20 (3.27), N 9.25 (9.36) %, **8** (Ln = Ho): C 40.90 (41.11), H 3.17 (3.12), N 9.18 (9.33) %, **9** (Ln = Er): C 40.78 (40.70), H 3.17 (3.12), N 9.15 (9.38) %, **10** (Ln = Yb): C 40.77 (41.00), H 3.14 (3.09), N 9.08 (9.14) %, **11** (Ln = Y): C 45.42 (45.67), H 3.53 (3.39), N 10.19 (10.32) %. The IR spectra of these complexes are almost superimposable with the spectrum of **7**_Dy with a maximum wave number difference of ±3 cm^{-1}.

3.4. Synthesis of the Representative Complex [Dy(NO$_3$)$_3$(salanH)$_2$(MeOH)]· (salanH) (**18**_Dy)

To a stirred yellow solution of salanH (0.17 g, 0.1 mmol) in MeOH (5 mL), solid Dy(NO$_3$)$_3$·5H$_2$O (0.31 g, 0.1 mmol) was added. The solid soon dissolved and the resulting yellowish orange solution was stirred for a further 10 min and stored in a closed flask at room temperature. X-ray quality, orange-brown crystals of the product were precipitated within 2 days. The crystals were collected by filtration, washed with cold MeOH (1 mL) and Et$_2$O (4 × 2 mL), and dried in air. The yield was 47% (based on the ligand available). Anal. calc. for C$_{40}$H$_{37}$N$_6$O$_{13}$Dy (found values in parentheses): C 49.41 (49.57), H 3.84 (3.76), N 8.65 (8.73) %. IR bands (KBr, cm^{-1}): 3420wb, 3062w, 1638s, 1618m, 1598s, 1534s, 1490s, 1458m, 1452sh, 1384m, 1302sh, 1284s, 1238m, 1182m, 1142s, 1120w, 1022s, 906m, 886w, 842sh, 832w, 814w, 786w, 760sh, 754s, 736sh, 682m, 578m, 554m, 514m, 504m, and 458m.

3.5. Syntheses of [Pr(NO₃)₃(salanH)₂(MeOH)]·(salanH) (12_Pr), [Nd(NO₃)₃(salanH)₂(MeOH)]· (salanH) (13_Nd), [Sm(NO₃)₃(salanH)₂(MeOH)]· (salanH) (14_Sm), [Eu(NO₃)₃(salanH)₂(MeOH)]· (salanH) (15_Eu), [Gd(NO₃)₃(salanH)₂(MeOH)]· (salanH) (16_Gd), [Tb(NO₃)₃(salanH)₂(MeOH)]· (salanH) (17_Tb), [Ho(NO₃)₃(salanH)₂(MeOH)]· (salanH) (19_Ho), [Er(NO₃)₃(salanH)₂(MeOH)]· (salanH) (20_Er), [Yb(NO₃)₃(salanH)₂(MeOH)]· (salanH) (21_Yb) and [Y(NO₃)₃(salanH)₂(MeOH)]· (salanH) (22_Y)

These complexes were prepared in an identical manner with **18**_Dy by simply by replacing $Dy(NO_3)_3 \cdot 5H_2O$ with the equivalent amount of the appropriate $Ln(NO_3)_3 \cdot xH_2O$ starting material (x = 5 or 6). Typical yields were in the 40% to 50% range (based on salanH). Anal. calc. for $C_{40}H_{37}N_6O_{13}Ln$ (found values in parentheses): **12** (Ln = Pr): C 50.53 (51.12), H 3.93 (4.06), N 8.84 (8.76) %; **13** (Ln = Nd): C 50.35 (49.70), H 3.92 (3.95), N 8.81 (8.82) %; **14** (Ln = Sm): C 50.03 (50.36), H 3.89 (3.79), N 8.75 (8.61) %; **15** (Ln = Eu): C 49.95 (50.13), H 3.89 (3.96), N 8.74 (8.81) %; **16** (Ln = Gd): C 49.68 (50.08), H 3.86 (3.78), N 8.69 (8.78) %; **17** (Ln = Tb): C 49.59 (49.73), H 3.86 (3.97), N 8.68 (8.40) %; **19** (Ln = Ho): C 49.28 (49.11), H 3.83 (3.71), N 8.62 (8.56) %; **20** (Ln = Er): C 49.17 (49.51), H 3.82 (3.86), N 8.60 (8.81) %; **21** (Ln = Yb): C 48.88 (49.13), H 3.80 (3.73), N 8.55 (8.79) %; **22** (Ln = Y): C 53.45 (52.99), H 4.16 (4.11), N 9.35 (9.20) %. The IR spectra of **12**_Pr-**17**_Tb and **19**_Ho-**22**_Y are almost superimposable with the spectrum of **18**_Dy with a maximum wave number difference of ± 5 cm^{-1}.

3.6. Single-Crystal X-ray Crystallography

Suitable orange crystals of **4**·MeCN_Eu (0.06 × 0.25 × 0.34 mm), **7**·MeCN_Dy (0.11 × 0.20 × 0.37 mm), **10**·MeCN_Yb (0.04 × 0.15 × 0.20 mm), **17**_Tb (0.05 × 0.13 × 0.22 mm), and an orange-brown crystal of **18**_Dy (0.06 × 0.07 × 0.22 mm) were taken from the mother liquor and immediately cooled to −103 °C for **4**·MeCN_Eu and −113 °C for the other complexes. Diffraction data were collected on a Rigaku R-AXIS SPIDER Image Plate diffractometer using graphite-monochromated Mo Kα (**4**·MeCN_Eu, **10**·MeCN_Tb) or Cu Kα (**7**·MeCN_Dy, **17**_Tb, **18**_Dy) radiations. Data collection (ω-scans) and processing (cell refinement, data reduction, and empirical absorption correction) were performed using the CrystalClear program package [93]. The structures were solved by direct methods using SHELXS, ver. 2013/1 [94] and refined by full-matrix least-squares techniques on F^2 with SHELXL, ver. 2014/6 [95]. All non-H atoms were refined anisotropically. The H atoms in the five structures were either located by difference maps and refined isotropically or were introduced at calculated positions and refined as riding on their corresponding bonded atoms. Plots of the structures were drawn using the Diamond 3 program package [96]. Important crystallographic data are listed in Table S5. Full details can be located in the CIF files.

The X-ray crystallographic data for the complexes have been deposited with CCDC (reference numbers CCDC 1863571, 1863570, 1863572, 1863568, and 1863569 for **4**·MeCN_Eu, **7**·MeCN_Dy, **10**·MeCN_Tb, **17**_Tb, and **18**_Dy, respectively). They can be obtained free of charge at http://www.ccdc.cam.ac.uk/conts/retrieving.html or from the Cambridge Crystallographic Data Center, 12 Union Road, Cambridge, CB2 1EZ, UK: Fax: +44-1223-336033; or e-mail: deposit@ccdc.cam.ac.uk.

4. Conclusions and Perspectives

It is difficult to conclude on a research project that is still at its infancy. We believe that we have partly fulfilled the three goals mentioned in Section 1 (Introduction). In detail: (i) The first use of the bidentate anil ligand salanH ($R_1 = R_2$ = H in Scheme 1) has provided access to two families of mononuclear Ln(III) complexes depending on the reaction solvent used. The members of the two molecules have exciting structural features (both molecular and supramolecular) including an extremely rare coordination mode of the salanH ligands in both families, the presence of a lattice salanH molecule in the [Ln(NO₃)₃(salanH)₂(MeOH)]·(salanH) family (**12**–**22**), the formation of doubly H-bonded dimers in the [Ln(NO₃)₃(salanH)₂(H₂O)]·MeCNcomplexes (**1**–**11**), and the different spatial disposition ("*cis*" in **1**–**11** vs. "*trans*" in **12**–**22**) of the coordinated salanH ligands. The coordination chemistry of salanH towards Ln(III) ions is distinctly different from the recently reported [57] coordination chemistry of 5BrsalanH (R_1 = Br and R_2 = H in Scheme 1). For example, while complexes

[Ln(NO$_3$)$_3$(salanH)$_2$(H$_2$O)]·MeCN (present work) and [Ln(NO$_3$)$_3$(5BrsalanH)$_2$(H$_2$O)]·MeCN [57] have the same chemical composition, their molecular and supramolecular structures differ (*vide supra*). (ii) The Tb(III) compound **17_Tb** and the Dy(III) complexes **7_Dy** and **18_Dy** show field-induced slow magnetic relaxation properties. The enhanced/improved properties of **17_Tb** and **18_Dy** compared with those of **6_Tb** and **7_Dy** have been nicely correlated with the different supramolecular characteristics of the two families and (iii) the complexes exhibit ligand-based green photoluminescence at room-temperature while near-IR, Ln(III)-based emission has been recorded for the Pr(III), Nd(III), Sm(III), Er(III), and Yb(III) members of the two families. Complexes **7_Dy**, **17_Tb**, and **18_Dy** can be considered as compounds that exhibit both photoluminescence (albeit not derived from the 4f-metal ions) and field-induced slow magnetic relaxation by combining the two properties within the same molecule. We are still far from our ultimate goal of correlating optical and magnetic properties since it has been performed in an elegant way by other groups [44,46–49].

Our future efforts in the present general project are directed towards: (a) Synthetic, structural, optical, and magnetic studies of complex [Dy(NO$_3$)$_3$(salanH)$_2$(MeOH)] (mentioned in the "Supplementary Materials" section) and its analogues with other 4f-metal ions. (b) The preparation of mononuclear Ln(III) complexes with other anil-type ligands (R$_1$, R$_2$ = various non-donor groups in Scheme 1) with the goals to see if there are other structural types in this chemistry (for example, if a bidentate chelating coordination mode of the ligands can be realized), isolate complexes with zero-field SIM properties (for example, using bulkier anils to lower the coordination number of the Ln^{III} center) and to achieve Ln^{III}-based emission with the organic ligand acting as an "antenna" (for example, enhancing the aromatic content of the ligands in order to realize efficient organic ligand-to-Ln^{III} energy transfer). All these efforts, which are already well advanced, are in progress and results will be reported in due course. Lastly, we have been working intensely to realize our long-term goal to achieve Dy^{III}-based emission in a SIM. This will enable us to correlate luminescence and magnetism since the highest f-f transition in the emission spectra can provide a direct picture of the splitting of the ground *J* multiplet.

Author Contributions: I.M.-M. and D.M. contributed toward the syntheses, crystallization, and conventional characterization of the complexes. Both also contributed to the interpretation of the results. J.M. and A.E. performed the magnetic measurements, interpreted the results, and calculated the magnetic anisotropy axes of the Dy^{III} centers in complex **7**·MeCN_Dy and **18_Dy**. The latter also wrote the relevant part of the paper. L.C. and S.C. carried out the solid-state, room-temperature visible and near-IR emission studies upon CW laser excitation at 405 nm and interpreted the results. The latter also wrote the relevant part of the paper. V.B. performed the solid-state, room-temperature visible emission studies (including the recording of the excitation spectra), interpreted the results, and wrote the relevant part of the paper. C.P.R. and V.P. collected single-crystal X-ray crystallographic data, solved the structures, and performed the refinement of the structures. The latter also recorded pXRD patterns, studied in detail the supramolecular features of the crystal structures, and wrote the relevant part of the paper. S.P.P. coordinated the research, contributed to the interpretation of the results, and wrote the paper based on the

reports of his collaborators. All the authors exchanged opinions concerning the interpretation of the results and commented on the manuscript at all stages.

Conflicts of Interest: The authors declare no conflicts of interest.

References and Notes

1. Kahn, O. *Molecular Magnetism*; VCH Publishers: New York, NY, USA, 1993.
2. Caneschi, A.; Gatteschi, D.; Sessoli, R.; Barra, A.L.; Brunel, L.C.; Guillot, M. Alternating Current Susceptibility, High Field Magnetization, and Millimeter Band EPR Evidence for a ground S=10 State in [Mn$_{12}$O$_{12}$(CH$_3$COO)$_{16}$(H$_2$O)$_4$]·2CH$_3$COOH·4H$_2$O. *J. Am. Chem. Soc.* **1991**, *113*, 5873–5874. [CrossRef]
3. For a review on Mn Single-Molecule Magnets, see: Bagai, R.; Christou, G. The drosophila of single-molecule magnetism: [Mn$_{12}$O$_{12}$(O$_2$CR)$_{16}$(H$_2$O)$_4$]. *Chem. Soc. Rev.* **2009**, *38*, 1011–1026. [CrossRef] [PubMed]
4. For an excellent comprehensive review, see: Milios, C.J.; Winpenny, R.E.P. Cluster-Based Single-Molecule Magnets. *Struct. Bond.* **2015**, *164*, 1–109.
5. For an excellent comprehensive review, see: Woodruff, D.N.; Winpenny, R.E.P.; Layfield, R.A. Lanthanide Single-Molecule Magnets. *Chem. Rev.* **2013**, *113*, 5110–5148. [CrossRef] [PubMed]
6. Liu, J.-L.; Chen, Y.-C.; Tong, M.-L. Symmetry strategies for high performance lanthanide-based single-molecule magnets. *Chem. Soc. Rev.* **2018**, *47*, 2431–2453. [CrossRef] [PubMed]
7. Guo, Y.-N.; Xu, G.-F.; Guo, Y.; Tang, J. Relaxation dynamics of dysprosium(III) single-molecule magnets. *Dalton Trans.* **2011**, *40*, 9953–9963. [CrossRef] [PubMed]
8. Liddle, S.T.; Van Slageren, J. Improving f-element single molecule magnets. *Chem. Soc. Rev.* **2015**, *44*, 6655–6669. [CrossRef] [PubMed]
9. Zhang, P.; Zhang, L.; Tang, J. Hydrazone-based Dysprosium Single Molecule Magnets. *Current Inorg. Chem.* **2013**, *3*, 101–111. [CrossRef]
10. Zhang, P.; Guo, Y.-N.; Tang, J. Recent advances in dysprosium-based single molecule magnets: Structural overview and synthetic strategies. *Coord. Chem. Rev.* **2013**, *257*, 1728–1763. [CrossRef]
11. Zhang, P.; Zhang, L.; Tang, J. Lanthanide single molecule magnets: Progress and perspective. *Dalton Trans.* **2015**, *44*, 3923–3929. [CrossRef] [PubMed]
12. Pedersen, K.S.; Woodruff, D.N.; Bendix, J.; Clérac, R. Experimental Aspects of Lanthanide Single-Molecule Magnet Physics. In *Lanthanides and Actinides in Molecular Magnetism*, 1st ed.; Layfield, R.A., Murugesu, M., Eds.; Wiley-VCH: Berlin, Germany, 2015; pp. 125–152.
13. Habib, F.; Murugesu, M. Lessons learned from dinuclear lanthanide nano-magnets. *Chem. Soc. Rev.* **2013**, *42*, 3278–3288. [CrossRef] [PubMed]
14. Luzon, J.; Sessoli, R. Lanthanides in molecular magnetism: So fascinating, so challenging. *Dalton Trans.* **2012**, *41*, 13556–13567. [CrossRef] [PubMed]
15. Gupta, S.K.; Murugavel, R. Enriching lanthanide single-ion magnetism through symmetry and axiality. *Chem. Commun.* **2018**, *54*, 3685–3696. [CrossRef] [PubMed]
16. Rinehart, J.D.; Long, J.R. Exploiting single-ion anisotropy in the design of f-element single-molecule magnets. *Chem. Sci.* **2011**, *2*, 2078–2085. [CrossRef]
17. Pointillant, F.; Cador, O.; Le Guennic, B.; Quahab, L. Uncommon lanthanide ions in purely 4f Single Molecule Magnets. *Coord. Chem. Rev.* **2017**, *346*, 150–175. [CrossRef]
18. Ishikawa, N.; Sujita, M.; Ishikawa, T.; Koshihara, S.-Y.; Kaizu, Y. Lanthanide Double-Decker Complexes Functioning as Magnets at the Single-Molecular Level. *J. Am. Chem. Soc.* **2003**, *125*, 8694–8695. [CrossRef] [PubMed]
19. Coutinho, J.T.; Monteiro, B.; Pereira, L.C.J. Ln(III)-based SIMs. In *Lanthanide-Based Multifunctional Materials*, 1st ed.; Martin-Ramos, P., Ramos-Silva, M., Eds.; Elsevier: Amsterdam, The Netherlands, 2018; pp. 195–231.

20. Gupta, S.K.; Rajeshkumar, T.; Rajaraman, G.; Murugavel, R. Is a strong axial crystal-field the only essential condition for a large magnetic anisotropy barrier? The case of non-Kramers Ho(III) versus Tb(III). *Dalton Trans.* **2018**, *47*, 357–366. [CrossRef] [PubMed]

21. Xu, M.-X.; Meng, Y.-S.; Xiong, J.; Wang, B.-W.; Jiang, S.-D.; Gao, S. Magnetic anisotropy investigation on light lanthanide complexes. *Dalton Trans.* **2018**, *47*, 1966–1971. [CrossRef] [PubMed]

22. Ishikawa, R.; Michiwaki, S.; Noda, T.; Katoh, K.; Yamashita, M.; Matsubara, K.; Kawata, S. Field-Induced Slow Magnetic Relaxation of Mono- and Dinuclear Dysprosium(III) Complexes Coordinated by a Chloranilate with Different Resonance Forms. *Inorganics* **2018**, *6*, 7. [CrossRef]

23. Harriman, K.L.M.; Brosmer, J.L.; Ungur, L.; Diaconescu, P.L.; Murugesu, M. Pursuit of Record Breaking Energy Barriers: A Study of Magnetic Axiality in Diamide Ligated Dy^{III} Single-Molecule Magnets. *J. Am. Chem. Soc.* **2017**, *139*, 1420–1423. [CrossRef] [PubMed]

24. Liu, J.; Chen, Y.-C.; Jia, J.-H.; Liu, J.-L.; Vieru, V.; Ungur, L.; Chibotaru, L.F.; Lan, Y.; Wernsdorfer, W.; Gao, S.; et al. A Stable Pentagonal-Bipyramidal Dy(III) Single-Ion Magnet with a Record Magnetization Reversal Barrier over 1000 K. *J. Am. Chem. Soc.* **2016**, *138*, 5441–5450. [CrossRef] [PubMed]

25. Chen, Y.-C.; Liu, J.-L.; Wernsdorfer, W.; Liu, D.; Chibotaru, L.F.; Chen, X.-M.; Tong, M.-L. Hyperfine-Interaction-Driven Suppression of Quantum Tunneling at Zero Field in a Holmium(III) Single-Ion Magnet. *Angew. Chem. Int. Ed.* **2017**, *56*, 4996–5000. [CrossRef] [PubMed]

26. Zhang, H.; Nakanishi, R.; Katoh, K.; Breedlove, B.K.; Kitagawa, Y.; Yamashita, M. Low coordinated mononuclear erbium(III) single-molecule magnets with C$_{3v}$ symmetry: A method for altering single-molecule magnet properties by incorporating hard and soft donors. *Dalton Trans.* **2018**, *47*, 302–305. [CrossRef] [PubMed]

27. Ungur, L.; Chibotaru, L.F. Strategies toward High-Temperature Lanthanide-Based Single-Molecule Magnets. *Inorg. Chem.* **2016**, *55*, 10043–10056. [CrossRef] [PubMed]

28. Chen, Y.-C.; Liu, J.-L.; Ungur, L.; Liu, J.; Li, Q.-W.; Wang, L.-F.; Ni, Z.-P.; Chibotaru, L.F.; Chen, X.-M.; Tong, M.-L. Symmetry Supported Magnetic Blocking at 20 K in the Pentagonal Bipyramidal Dy(III) Single-Ion Magnets. *J. Am. Chem. Soc.* **2016**, *138*, 2829–2837. [CrossRef] [PubMed]

29. Ding, Y.-S.; Chilton, N.F.; Winpenny, R.E.P.; Zheng, Y.-Z. On Approaching the Limit of Molecular Magnetic Anisotropy: A Near Perfect Pentagonal Bipyramidal Dysprosium (III) Single-Molecule Magnet. *Angew. Chem. Int. Ed.* **2016**, *55*, 16071–16074. [CrossRef] [PubMed]

30. Guo, M.; Tang, J. Six-Coordinate Ln(III) Complexes with Various Coordination Geometries Showing Distinct Magnetic Properties. *Inorganics* **2018**, *6*, 16. [CrossRef]

31. Dickie, C.M.; Laughlin, A.L.; Wofford, J.D.; Bhuvanech, N.S.; Nippe, M. Transition metal redox switches for reversible "on/off" and "slow/fast" single-molecule magnet behavior in dysprosium and erbium bis-diamidoferrocene complexes. *Chem. Sci.* **2017**, *8*, 8039–8049. [CrossRef] [PubMed]

32. Cucinotta, G.; Perfetti, M.; Luzon, J.; Etienne, M.; Car, P.-E.; Caneschi, A.; Calvez, G.; Bernot, K.; Sessoli, R. Magnetic Anisotropy in a Dysprosium/DOTA Single-Molecule Magnet: Beyond Simple Magneto-Structural Correlations. *Angew. Chem. Int. Ed.* **2012**, *51*, 1606–1610. [CrossRef] [PubMed]

33. Ghosh, S.; Datta, S.; Friend, L.; Cardonna-Serra, S.; Gaita-Ariño, A.; Coronado, E.; Hill, S. Multi-frequency EPR studies of a mononuclear holmium single-molecule magnet based on the polyoxometalate [Ho^{III}(W$_5$O$_{18}$)$_2$]$^{9-}$. *Dalton Trans.* **2012**, *41*, 13697–13704. [CrossRef] [PubMed]

34. Guo, F.-S.; Day, B.M.; Chen, Y.-C.; Tong, M.-L.; Mansikkamäki, A.; Layfield, R.A. A Dysprosium Metallocene Single-Molecule Manget Functioning at the Axial Limit. *Angew. Chem. Int. Ed.* **2017**, *56*, 11445–11449. [CrossRef] [PubMed]

35. Goodwin, C.A.P.; Ortu, F.; Reta, D.; Chilton, N.F.; Mills, D.P. Molecular magnetic hysteresis at 60 Kelvin in dysprosocenium. *Nature* **2017**, *548*, 439–442. [CrossRef] [PubMed]

36. Goodwin, C.A.P.; Reta, D.; Ortu, F.; Chilton, N.F.; Mills, D.P. Synthesis and Electronic Structures of Heavy Lanthanide Metallocenium Cations. *J. Am. Chem. Soc.* **2017**, *139*, 18714–18724. [CrossRef] [PubMed]

37. Bunzli, J.-C.G. On the design of highly luminescent lanthanide complexes. *Coord. Chem. Rev.* **2015**, *293–294*, 19–47. [CrossRef]

38. Swavey, S.; Swavey, R. Dinuclear and polynuclear lanthanide coordination complexes containing polyazine ligands: Synthesis and luminescent properties. *Coord. Chem. Rev.* **2009**, *253*, 2627–2638. [CrossRef]

39. Bunzli, J.-C.G.; Piguet, C. Taking advantage of luminescent lanthanide ions. *Chem. Soc. Rev.* **2005**, *34*, 1048–1077. [CrossRef] [PubMed]

40. He, H. Near-infrared emitting lanthanide complexes of porphyrin and BODIPY dyes. *Coord. Chem. Rev.* **2014**, *273–274*, 87–99. [CrossRef]

41. Ahmed, Z.; Iftikhar, K. Sensitization of Visible and NIR Emitting Lanthanide(III) Ions in Noncentrosymmetric Complexes of Hexafluoroacetylacetone and Unsubstituted Monodentate Pyrazole. *J. Phys. Chem. A* **2013**, *117*, 11183–11201. [CrossRef] [PubMed]

42. Rizzo, F.; Papagni, A.; Meinardi, F.; Tubino, R.; Ottonelli, M.; Musso, G.F.; Dellepione, G. Novel lanthanide complexes for visible and IR emission. *Synth. Met.* **2004**, *147*, 143–147. [CrossRef]

43. Stacey, O.J.; Ward, B.D.; Amoroso, A.J.; Pope, S.J.A. Near-IR luminescent lanthanide complexes with 1,8-diaminoanthraquinone-based chromophoric ligands. *Dalton Trans.* **2016**, *45*, 6674–6681. [CrossRef] [PubMed]

44. For an excellent paper covering the whole literature, see: Mamontova, E.; Long, J.; Ferreira, R.A.S.; Botas, A.M.P.; Luneau, D.; Guari, Y.; Carlos, L.D.; Larionova, J. Magneto-Luminescence Correlation in the Textbook Dysprosium(III) Nitrate Single-Ion Magnet. *Magnetochemistry* **2016**, *2*, 41. [CrossRef]

45. Fondo, M.; Corredoira-Vázquez, J.; Herrera-Lanzós, A.; Garcia-Deibe, A.M.; Sanmartin-Matalobos, J.; Herrera, J.M.; Colacio, E.; Nuñez, C. Improving the SMM and luminescence properties of lanthanide complexes with LnO$_9$ cores in the presence of Zn^{II}: An emissive Zn$_2$Dy single ion magnet. *Dalton Trans.* **2017**, *46*, 17000–17009, and refs. cited therein. [CrossRef] [PubMed]

46. Long, J.; Vallat, R.; Ferreira, R.A.S.; Carlos, L.D.; Almeida Paz, F.A.; Guari, Y.; Larionova, J. A bifunctional luminescent single-ion magnet: Towards correlation between luminescence studies and magnetic slow relaxation processes. *Chem. Commun.* **2012**, *48*, 9974–9976. [CrossRef] [PubMed]

47. Yamashita, K.; Miyazaki, R.; Kataoka, Y.; Nakanishi, T.; Hasegawa, Y.; Nakano, M.; Yamasura, T.; Kajiwara, T. A luminescent single-molecule magnet: Observation of magnetic anisotropy using emission as a probe. *Dalton Trans.* **2013**, *42*, 1987–1990. [CrossRef] [PubMed]

48. Pointillart, F.; Le Guennic, B.; Colhen, S.; Cador, O.; Maury, O.; Quahab, L. A redox-active luminescent ytterbium-based single molecule magnet. *Chem. Commun.* **2013**, *49*, 615–617. [CrossRef] [PubMed]

49. Gavey, E.L.; Al Hareri, M.; Regier, J.; Carlos, L.D.; Ferreira, R.A.S.; Razavi, F.S.; Rawson, J.M.; Pilkington, M. Placing a crown on Dy(III)-A dual property Ln^{III} crown ether complex displaying optical properties and SMM behaviour. *J. Mater. Chem. C* **2015**, *3*, 7738–7747. [CrossRef]

50. For example, see: Anastasiadis, N.C.; Kalofolias, D.A.; Philippidis, A.; Tzani, S.; Raptopoulou, C.P.; Psycharis, V.; Milios, C.J.; Escuer, A.; Perlepes, S.P. A family of dinuclear lanthanide(III) complexes from the use of a tridentate Schiff base. *Dalton Trans.* **2015**, *44*, 10200–10209. [CrossRef] [PubMed]

51. For example, see: Mylonas-Margaritis, I.; Mayans, J.; Sakellakou, S.-M.; Raptopoulou, C.P.; Psycharis, V.; Escuer, A.; Perlepes, S.P. Using the Singly Deprotonated Triethanolamine to Prepare Dinuclear Lanthanide(III) Complexes: Synthesis, Structural Characterization and Magnetic Studies. *Magnetochemistry* **2017**, *3*, 5. [CrossRef]

52. For example, see: Anastasiadis, N.C.; Granadeiro, C.M.; Klouras, N.; Cunha-Silva, L.; Raptopoulou, C.P.; Psycharis, V.; Bekiari, V.; Balula, S.S.; Escuer, A.; Perlepes, S.P. Dinuclear Lanthanide(III) Complexes by Metal-Ion-Assisted Hydration of Di-2-pyridyl Ketone Azine. *Inorg. Chem.* **2013**, *52*, 4145–4147. [CrossRef] [PubMed]

53. For example, see: Bekiari, V.; Thiakou, K.A.; Raptopoulou, C.P.; Perlepes, S.P.; Lianos, P. Structure and photophysical behavior of 2,2′-bipyrimidine/lanthanide ion complexes in various environments. *J. Lumin.* **2008**, *128*, 481–488. [CrossRef]

54. For example, see: Mylonas-Margaritis, I.; Kitos, A.A.; Panteli, C.C.; Skordi, K.; Tasiopoulos, A.J.; Bekiari, V.; Escuer, A.; Perlepes, S.P. 2-hydroxybenzophenone-controlled self-assembly of enneanuclear lanthanide(III) hydroxo coordination clusters with an "hourglass"-like topology. *Inorg. Chem. Commun.* **2017**, *83*, 118–122. [CrossRef]

55. For example, see: Nikolaou, H.; Terzis, A.; Raptopoulou, C.P.; Psycharis, V.; Bekiari, V.; Perlepes, S.P. Unique Dinuclear, Tetrakis(nitrato-O,O′)-Bridged Lanthanide(III) Complexes from the Use of Pyridine-2-Amidoxime: Synthesis, Structural Studies and Spectroscopic Characterization. *J. Surf. Interface Mater.* **2014**, *2*, 311–318. [CrossRef]

56. For example, see: Anastasiadis, N.C.; Mylonas-Margaritis, I.; Psycharis, V.; Raptopoulou, C.P.; Kalofolias, D.A.; Milios, C.J.; Klouras, N.; Perlepes, S.P. Dinuclar, tetrakis(acetato)-bridged lanthanide(III) complexes form the use of 2-acetylpyridine hydrazone. *Inorg. Chem. Commun.* **2015**, *51*, 99–102. [CrossRef]

57. Maniaki, D.; Mylonas-Margaritis, I.; Mayans, J.; Savvidou, A.; Raptopoulou, C.P.; Bekiari, V.; Psycharis, V.; Escuer, A.; Perlepes, S.P. Slow magnetic relaxation and luminescence properties in lanthanide(III)/anil complexes. *Dalton Trans.* **2018**, *47*, 11859–11872. [CrossRef] [PubMed]

58. Yamada, S. Advancement in stereochemical aspects of Schiff base metal complexes. *Coord. Chem. Rev.* **1999**, *190–192*, 537–555. [CrossRef]

59. Nematirad, M.; Gee, W.J.; Langley, S.K.; Chilton, N.F.; Moubaraki, B.; Murray, K.S.; Batten, S.R. Single molecule magnetism in a μ-phenolato dinuclear motif ligated by heptadentate Schiff base ligands. *Dalton Trans.* **2012**, *41*, 13711–13715. [CrossRef] [PubMed]

60. Lacelle, T.; Brunet, G.; Pialat, A.; Holmberg, R.J.; Lan, Y.; Gabidullin, B.; Korobkov, I.; Wernsdorfer, W.; Murugesu, M. Single-molecule magnet behaviour in a tetranuclear Dy^{III} complex formed from a novel tetrazine-centered hydrazone Schiff base ligand. *Dalton Trans.* **2017**, *46*, 2471–2478. [CrossRef] [PubMed]

61. Guo, Y.-N.; Xu, G.-F.; Wernsdorfer, W.; Ungur, V.; Guo, Y.; Tang, J.; Zhang, H.-J.; Chibotaru, L.F.; Powell, A.K. Strong axiality and Ising Exchange Interaction Suppress Zero-Field Tunneling of Magnetization of an Asymmetric Dy$_2$ Single-Molecule Magnet. *J. Am. Chem. Soc.* **2011**, *133*, 11948–11951. [CrossRef] [PubMed]

62. For a comprehensive review, see: Hadjoudis, E.; Mavridis, I.M. Photochromism and thermochromism of Schiff bases in the solid state: Structural aspects. *Chem. Soc. Rev.* **2004**, *33*, 579–588. [PubMed]

63. For a review, see: Hadjoudis, E. Photochromic and Thermochromic Anils. *Mol. Eng.* **1995**, *5*, 301–337. [CrossRef]

64. Shen, M.Y.; Zhao, L.Z.; Goto, T.; Mordzinski, A. Polarization dependence of photochromism in a N-salicylideneaniline. *J. Chem. Phys.* **2000**, *112*, 2490–2497. [CrossRef]

65. Harada, J.; Uekusa, H.; Ohashi, Y. X-ray Analysis of Structural Changes in Photochromic Salicylidene Crystals. Solid-State Reaction Induced by Two-Photon Excitation. *J. Am. Chem. Soc.* **1999**, *121*, 5809–5810. [CrossRef]

66. Wei, L.; Stogsdill, R.M.; Lingafelter, E.C. The crystal structure of bis-(N-phenylsalicylaldiminato)copper(II). *Acta Crystallogr.* **1964**, *17*, 1058–1062. [CrossRef]

67. Sadikov, G.G.; Tkachev, V.V.; Antsyshkina, A.S.; Sergienko, V.S.; Burlov, A.S.; Vasil'chenko, I.S.; Garnovskii, A.D. Coordination compounds of metals with azomethine ligands: The crystal and molecular structure of a zinc complex with 2-hydroxy-1-naphthalidene-aniline. *Russ. J. Inorg. Chem.* **2005**, *50*, 353–359.

68. Van Wyk, J.L.; Mapolie, S.F.; Lennartson, A.; Håkansson, M.; Jagner, S. The catalytic oxidation of phenol in aqueous media using cobalt(II) complexes derived from N-(aryl) salicylaldimines. *Inorg. Chim. Acta* **2008**, *361*, 2094–2100. [CrossRef]

69. McAuliffe, C.A.; Pritchard, R.G.; Luaces, L.; Garcia-Vazquez, J.A.; Romero, J.; Bermejo, M.R.; Sousa, A. Chlorobis(N-phenylsalicylideneaminato-O,N)manganese(III): A Manganese Schiff-Base Complex Derived by an Electrochemical Route. *Acta Crystallogr.* **1993**, *C49*, 587–589. [CrossRef]

70. Jones, M.D.; Davidson, M.G.; Keir, C.G.; Hughes, L.M.; Mahon, M.F.; Apperley, D.C. Zinc(II) Homogeneous and Heterogeneous Species and Their Application for the Ring-Opening Polymerization of rac-Lactide. *Eur. J. Inorg. Chem.* **2009**, 635–642. [CrossRef]

71. Ren, K.; Shang, X.; Fu, J.; Zhao, P.; Zhang, J. Copper complex based on 2-(phenylimino-methyl)-phenol as a high selective fluorescent probe for hydrogen sulfide. *Polyhedron* **2016**, *104*, 99–105. [CrossRef]

72. Jain, A.K.; Gupta, A.; Bohra, R.; Lorenz, I.-P.; Mayer, P. Synthesis and structural elucidation of some novel aluminium(III) complexes with Schiff bases: Crystal and molecular structure of [Al{O(C$_6$H$_4$)CH=NC$_6$H$_5$}$_2${HO(C$_6$H$_4$)CH=NC$_6$H$_5$}$_2$]Br. *Polyhedron* **2006**, *25*, 654–662. [CrossRef]

73. Yue, S.; Li, J.; Zang, S.-L.; Gu, X.-J.; Yu, Y.-J.; Jin, H. Schiff Base Complex of Gallium: Synthesis and Crystal Structure. *Chin. J. Inorg. Chem.* **2010**, *26*, 763–768.

74. Zhou, M.-D.; Zhao, J.; Li, J.; Yue, S.; Bao, C.-N.; Mink, J.; Zang, S.-L.; Kühn, F.E. MTO Schiff-Base Complexes: Synthesis, Structures and Catalytic Applications in Olefin Epoxidation. *Chem. Eur. J.* **2007**, *13*, 158–166. [CrossRef] [PubMed]

75. Destro, R.; Gavezzotti, A.; Simonetta, M. Salicylideneaniline. *Acta Crystallogr.* **1978**, *B34*, 2867–2869. [CrossRef]

76. Arod, F.; Gardon, M.; Pattison, P.; Chapuis, G. The α$_2$-polymorph of salicylideneaniline. *Acta Crystallogr.* **2005**, *C61*, o317–o320. [CrossRef] [PubMed]

77. Arod, F.; Pattison, P.; Schenk, K.J.; Chapuis, G. Polymorphism in N-Salicylideneaniline Reconsidered. *Cryst. Growth Des.* **2007**, *7*, 1679–1685. [CrossRef]

78. Kaur, G.; Singh, S.; Sreekumar, A.; Choudhury, A.R. The evaluation of the role of C-H···F hydrogen bonds in crystal altering the packing modes in the presence of strong hydrogen bond. *J. Mol. Struct.* **2016**, *1106*, 154–169. [CrossRef]

79. Camp, C.; Guidal, V.; Biswas, B.; Pécaut, J.; Dubois, L.; Mazzanti, M. Multielectron redox chemistry of lanthanide Schiff-base complexes. *Chem. Sci.* **2012**, *3*, 2433–2448. [CrossRef]

80. Pedersen, K.S.; Ariciu, A.-M.; McAdams, S.; Weihe, H.; Bendix, J.; Tuna, F.; Piligkos, S. Towards Molecular 4f Single-Ion Magnet Qubits. *J. Am. Chem. Soc.* **2016**, *138*, 5801–5804. [CrossRef] [PubMed]

81. Hussain, R.; Allodi, G.; Chiesa, A.; Garlatti, E.; Mitcov, D.; Konstantatos, A.; Pedersen, K.S.; De Renzi, R.; Piligkos, S.; Carretta, S. Coherent manipulation of a molecular Ln-based nuclear qubit coupled to an electron qubit. *J. Am. Chem. Soc.* **2018**, *140*, 9814–9818. [CrossRef] [PubMed]

82. Llunell, M.; Casanova, D.; Girera, J.; Alemany, P.; Alvarez, S. *SHAPE, Continuous Shape Measures Calculation*; Version 2.0; Universitat de Barcelona: Barcelona, Spain, 2010.

83. Alexandropoulos, D.I.; Fournet, A.; Cunha-Silva, L.; Mowson, A.M.; Bekiari, V.; Christou, G.; Stamatatos, T.C. Fluorescent Naphthalene Diols as Bridging Ligands in Ln^{III} Cluster Chemistry: Synthetic, Structural, Magnetic, and Photophysical Characterization of Ln^{III}_8 "Christmas Stars". *Inorg. Chem.* **2014**, *53*, 5420–5422. [CrossRef] [PubMed]

84. Sun, L.; Qiu, Y.; Liu, T.; Feng, J.; Deng, W.; Shi, L. Visible-near-infrared luminescent lanthanide ternary complexes based on beta-diketonate using visible-light excitation. *Luminescence* **2015**, *30*, 1071–1076. [CrossRef] [PubMed]

85. Reineke, S.; Baldo, M.A. Room temperature triplet state spectroscopy of organic semiconducors. *Sci. Rep.* **2014**, *4*, 3797. [CrossRef] [PubMed]

86. We thank one of the referees for her/his advice concerning the calculation of the triplet state of salanH.

87. Ning, Y.; Liu, Y.-W.; Meng, Y.-S.; Zhang, J.-L. Design of Near-Infrared Luminescent Lanthanide Complexes Sensitive to Environmental Stimulus through Rationally Tuning the Secondary Coordination Sphere. *Inorg. Chem.* **2018**, *57*, 1332–1341. [CrossRef] [PubMed]

88. Orbach, R. Spin-lattice relaxation in rare-earth salts. *Proc. R. Soc. Lond. A Math. Phys. Eng. Sci.* **1961**, *264*, 458–484. [CrossRef]

89. Bartolomé, J.; Filoti, G.; Kuncser, V.; Schienteie, G.; Mereacre, V.; Anson, C.E.; Powell, A.K.; Prodius, D.; Turta, C. Magnetostructural correlations in the tetranuclear series of {Fe_3LnO_2} butterfly core clusters: Magnetic and Mössbauer spectroscopic study. *Phys. Rev. B Condens. Matter Phys.* **2009**, *80*, 014430. [CrossRef]

90. Chilton, N.F.; Collison, D.; McInnes, E.J.L.; Winpenny, R.E.P.; Soncini, A. An electrostatic model for the determination of magnetic anisotropy in dysprosium complexes. *Nat. Commun.* **2013**, *4*, 2551–2557. [CrossRef] [PubMed]

91. Available online: http://www.nfchilton.com/magellan.html (accessed on 7 September 2018).

92. Kettle, S.F.A. *Physical Inorganic Chemistry—A Coordination Chemistry Approach*; Oxford University Press: Oxford, UK, 1998; pp. 462–465.

93. *CrystalClear*, ver. 1.40; Rigaku/MSC: The Woodlands, TX, USA, 2005.

94. Sheldrick, G.M. A short history of SHELX. *Acta Crystallogr.* **2008**, *A64*, 112–122. [CrossRef] [PubMed]

95. Sheldrick, G.M. Crystal structure refinement with SHELXL. *Acta Crystallogr.* **2015**, *C71*, 3–8.

96. *Diamond, Crystal and Molecular Structure Visualization*, ver. 3.1; Crystal Impact: Bonn, Germany, 2018.